

# **N** ISMIRM 2019 **NEWSLETTER**

***NUKEM Isotopes Imaging GmbH***

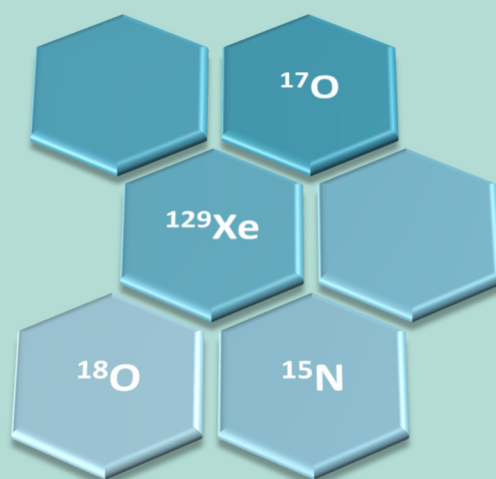
**Vol. # 3**

**P**roduct brochures of our isotopes

**O**xygen-17 ISMIRM abstracts

**X**enon-129 ISMIRM abstracts

**M**R-bibliography about Oxygen-17



Contact us



Company Video



[www.nukem-isotopes.com](http://www.nukem-isotopes.com)

<b>Company information .....</b>	<b>1</b>
<b>Company History .....</b>	<b>2</b>
General information about stable isotopes .....	2
<b>Our main imaging products .....</b>	<b>3</b>
Oxygen-17 .....	3
Xenon-129 .....	3
Nitrogen-15 .....	3
<b><sup>17</sup>Oxygen - product information .....</b>	<b>4</b>
Oxygen-17 in the form of Oxygen gas .....	4
Oxygen-17 in the form of water .....	5
Oxygen-17 in the form of D-Glucose .....	6
<b><sup>129</sup>Xenon - product information .....</b>	<b>7</b>
Xenon-129 in the form of gas mixtures and pure gas .....	7
<b><sup>15</sup>Nitrogen - product information .....</b>	<b>8</b>
Nitrogen-15 in the form of gas and salts for medical and agricultural applications .....	8
<b><sup>18</sup>Oxygen - product information .....</b>	<b>9</b>
Oxygen-18 in the form of water for medical applications .....	9
<b>Oxygen-17 ISMRM-abstracts .....</b>	<b>10</b>
ISMRM-abstract about Oxygen-17 in the form of gas .....	10
ISMRM-abstract ( <sup>17</sup> O in the form of D-Glucose) .....	21
<b>Xenon-129 ISMRM abstracts .....</b>	<b>23</b>
<b>Our ISMRM booth wall 2019 .....</b>	<b>31</b>
Information about our booth wall .....	31
<b>Oxygen-17 bibliography .....</b>	<b>32</b>
<b>Our cooperation partner .....</b>	<b>39</b>
Polarean Imaging plc .....	39
How does imaging with hyperpolarized Xe-129 work? .....	42
<b>Our ISMRM rubber duck family .....</b>	<b>43</b>

# Company information

**NUKEM Isotopes GmbH** based in Alzenau, Germany, is a global leader in providing enriched isotopes in the form of ultra-pure substances for industry, agriculture and medical applications. We have been a reliable partner for long term demands of stable isotopes for more than two decades. We maintain our partnership with the major enrichment enterprises in Europe, the Peoples Republic of China, the Republic of Georgia and the Russian Federation. With our warehouses at Frankfurt Airport, Hamburg seaport and cooperation partners in the USA, we are able to ship our isotopes within 48 hours to our clients worldwide. With our quality management (ISO 9001-2015, NUPIC) as well as third party analysis of our products, we guarantee our customers reliable services and high quality isotopes.

**NUKEM Isotopes Imaging GmbH** was established in 2015 and is specialized in the supply of stable isotopes, which are used in the field of Magnetic Resonance Imaging (MRI). Currently, NUKEM Isotopes Imaging GmbH provides two isotopes, **Oxygen-17** and **Xenon-129**, in different forms and enrichments. For further information, please check the following pages, visit our website ([www.nukem-isotopes.com](http://www.nukem-isotopes.com)) or contact us directly (ISMRM 2019, booth no.: 811). NUKEM Isotopes Imaging GmbH is ISO 9001-2015 certified and has established long term relationships with medical companies, who are specialized in producing ultra-pure products in compliance with cGMP regulations. This guarantees our customers in the medical fields a high quality and safe product.

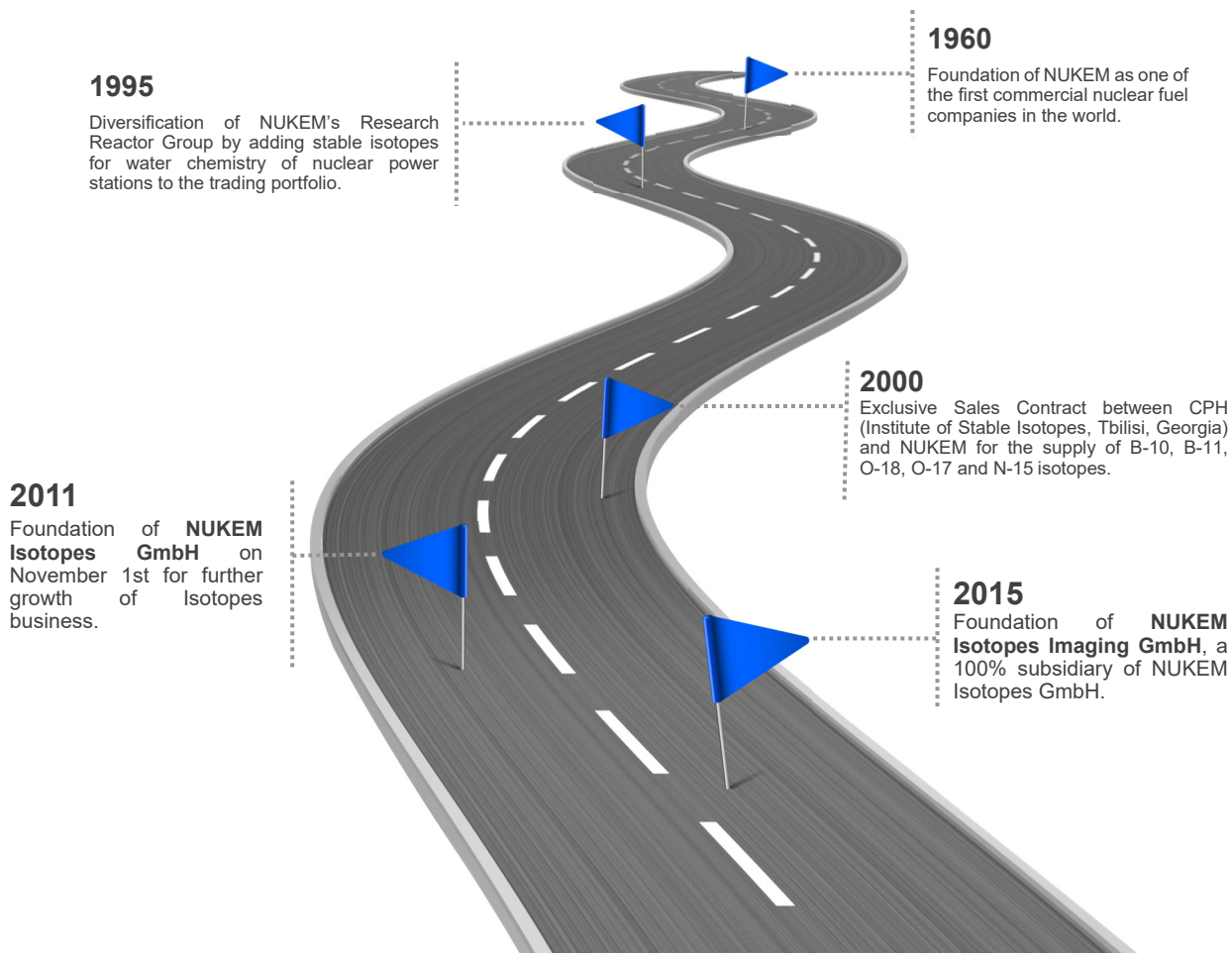


**2018 - We have moved!** In the course of our general expansion strategy, the company has decided to build a new, state of the art office building, in order to fulfil future needs. Now, after almost 12 months of intense planning- and construction work, we are very proud to announce the completion of this challenging project. With almost 1,000 m<sup>2</sup> of bright, modern offices, combined with functional storage- and packing

space, we are confident, we have established a good environment for our employees in order to ensure high quality services for our valued customers.

# Company History

## The History of NUKEM ...



## General information about stable isotopes




**Stable isotopes** are non-radioactive atoms of the same chemical element, which differ only in their number of neutrons. Therefore, they have nearly identical chemical behavior, but different physical properties. The nuclei with an odd number of protons and neutrons have a magnetic moment, which can be exploited by magnetic resonance technology.

In recent decades, stable isotopes empowered NMR/MRI technology to become an important tool in medical, agricultural and many other fields of research. As a global leader in providing highly enriched isotopes, NUKEM Isotopes Imaging GmbH is the perfect partner to help you realize your ideas with isotopes.

# Our main imaging products

## Our main isotopes for MRI and NMR

We supply the enriched stable isotopes Oxygen-17, Xenon-129 and Nitrogen-15 in different forms as ultra-pure substances. Below, you can learn more about the different forms, enrichments and applications of these isotopes.

		
<b><u>Oxygen-17</u></b> $^{17}\text{O}_2$ , $\text{H}_2^{17}\text{O}$	<b><u>Xenon-129</u></b> $^{129}\text{Xe}$ , $^{129}\text{Xe}$ / $\text{N}_2$ / He Mixtures	<b><u>Nitrogen-15</u></b> $^{15}\text{N}_2$ , $\text{Na}^{15}\text{NO}_3$ , $\text{K}^{15}\text{NO}_3$ , $^{15}\text{NH}_4\text{Cl}$ , $^{15}\text{NH}_4^{15}\text{NO}_3$ , $(^{15}\text{NH}_4)_2\text{SO}_4$
$^{17}\text{O}_2$ allows the non-invasive measurement of oxygen metabolism in tissues (mainly from the brain).	Hyperpolarized $^{129}\text{Xe}$ is used as non-radioactive, non-invasive MRI contrast agent for preparation of 3D lung images.	Used in agricultural research, hyperpolarized spectroscopic imaging and in many NMR research fields more.

## You need another enriched isotope?

If you are interested in isotopes other than those already mentioned above, please visit us at our ISMRM booth (#811). We are also available at any time by phone or email to answer your questions about our products or to provide you with a tailor-made offer. Further information about our product portfolio can also be found on our website ([www.nukem-isotopes.com](http://www.nukem-isotopes.com)).

*We would be happy to help you realize your future ideas.*

# <sup>17</sup>Oxygen - product information

## Oxygen-17 in the form of Oxygen gas

New developments with O-17 in the form of O<sub>2</sub> gas, enhance the quality of information about living tissue to improve the practice of medicine in the fields of cardiology and neurology among others.

The magnetic properties of O-17 make it a promising “tool” for assessment of in vivo metabolic tissue information at high fields ( $\geq 3T$ ).

The latest research results, performed with our 70at% enriched <sup>17</sup>O<sub>2</sub> gas can be found on the following pages (p.10-20).



Enrichment	<sup>17</sup> O $\geq$ 70at%
Purity	$\geq$ 99.9%
Volume	5L, 10L and 20L with a CGA 540 valve (left picture). 1L and 2L with a 1/4" NPT valve (right picture)
CO	$\leq$ 10 ppm
CO <sub>2</sub>	$\leq$ 100 ppm
H <sub>2</sub>	$\leq$ 50 ppm
N <sub>2</sub>	$\leq$ 500 ppm

***Our Oxygen-17 products are manufactured in accordance with cGMP regulations and with the requirements of 21 Code of Federal Regulations: PARTS 210 and 211.***

## Oxygen-17 in the form of water

Oxygen-17 ( $^{17}\text{O}$ ) in the form of water can be used in many fields of research. One example is the use as an MRI contrast agent for analysis of the brain cerebrospinal fluid (CSF). In addition,  $\text{H}_2^{17}\text{O}$  is the perfect precursor for the synthesis of NMR active molecules.

As a novel development, we have recently synthesized  $^{17}\text{O}$ -labeled D-Glucose from our  $^{17}\text{O}$ -enriched water. After successful application of the  $^{17}\text{O}$ -labeled D-Glucose, we are now convinced that there are several other molecules which can be synthesized from  $^{17}\text{O}$ -enriched water and can be used to study oxygen metabolic pathways by magnetic resonance technology.

If you are interested in our highly enriched water or  $^{17}\text{O}$ -labeled molecules, please do not hesitate to contact us. In cooperation with our synthesis partners, we will be able to provide you with a tailor-made offer.



Enrichment	$^{17}\text{O} \geq 10\text{at}\% - 90\text{at}\%$
Purity	$\geq 99.9\%$
Volumes	Available in various volumes. Please contact us.
pH	6 - 8

Al	$\leq 0,05^* \text{ ppm}$
Br	$\leq 0,5^* \text{ ppm}$
Ca	$\leq 0,1^* \text{ ppm}$
Cl	$\leq 0,5^* \text{ ppm}$
Co, Cr, Cu	$\leq 0,01^* \text{ ppm}$
F	$\leq 0,05^* \text{ ppm}$
Fe	$\leq 0,01^* \text{ ppm}$
K	$\leq 0,1^* \text{ ppm}$

Mg	$\leq 0,05^* \text{ ppm}$
Mn	$\leq 0,01^* \text{ ppm}$
Na	$\leq 1^* \text{ ppm}$
Ni	$\leq 0,01^* \text{ ppm}$
$\text{NO}_2$	$\leq 0,1^* \text{ ppm}$
$\text{NO}_3$	$\leq 0,05^* \text{ ppm}$
Si	$\leq 1^* \text{ ppm}$
$\text{SO}_4$	$\leq 0,1^* \text{ ppm}$
Pb	$\leq 0,01^* \text{ ppm}$
$\text{PO}_4$	$\leq 0,05^* \text{ ppm}$
Zn	$\leq 0,05^* \text{ ppm}$

\* applicable for 10at% enriched and 20at% enriched  $^{17}\text{O}$  water only!

***Our Oxygen-17 products are manufactured in accordance with cGMP regulations and with the requirements of 21 Code of Federal Regulations: PARTS 210 and 211.***

## Oxygen-17 in the form of D-Glucose

We are the first company in the world to synthesize substantial and high enriched amounts of single and double labelled Oxygen-17 D-Glucose. In cooperation with different research institutes, we performed the first in vivo tests with Oxygen-17 labeled D-Glucose. The results of the first experiments with Oxygen-17 labeled Glucose can be found in our ISMRM Newsletter from the last years (please visit our website for free download of the 2017 and 2018 edition).

The latest research results about the application of O-17 enriched D-Glucose can be found on the following pages (see p.21-22).



Enrichment (1)	$^{17}\text{O} \geq 35\text{at\%}$ at position 6 only
Enrichment (2)	$^{17}\text{O} \geq 65\text{at\%}$ at position 1 only
Enrichment (3)	Double labeled Glucose: $^{17}\text{O} \geq 35\text{at\%}$ at position 6 and $^{17}\text{O} \geq 65\text{at\%}$ at position 1
Purity	$\geq 95\%$

**We are also able to synthesize higher enrichments!**

Please contact us for further information.

***If you are interested in other enrichments (also labelled at other positions of the glucose) or in other molecules, labelled with Oxygen-17, please do not hesitate to contact us.***

# <sup>129</sup>Xenon - product information

## Xenon-129 in the form of gas mixtures and pure gas

Xenon-129 (Xe-129) in the hyperpolarized state is a revolutionary novel MRI contrast agent for diagnostically purposes. Xe-129 facilitates the taking of high-resolution 3D lung images by using a conventional MRI scanner.

Due to the varying solubility of Xenon in different environments, it is additionally possible to illuminate organ functions and tissue characteristics.

Our cooperation partner Polarean Imaging plc. designs and manufactures equipment for production of hyperpolarized Xenon-129. Further information about Polarean can be found in this Newsletter (see p. 39-42).

Enrichment	$^{129}\text{Xe} \geq 90\text{at\%}$ and $^{129}\text{Xe} \geq 80\text{at\%}$
Purity	All mixtures $\geq 99.9\%$
Volume/Valves	Mixtures: Available in 7,000 liter gas cylinder (with CGA 580 valve) Pure Gas: Available in 50 liter - 1,000 liter gas cylinder (with CGA 580 valve)
Composition	Standard mixture: $^{129}\text{Xe}$ - 1Vol%; $\text{N}_2$ - 10Vol%; He - 89Vol% (balance) Mixture (tailor made): $^{129}\text{Xe}$ – X Vol%; $\text{N}_2$ – X Vol%; He – X Vol% (balance) For other gas mixtures, please contact us.

CO	$\leq 1 \text{ ppm (mixtures) } / \leq 10 \text{ ppm (pure gas)}$
CO <sub>2</sub>	$\leq 1 \text{ ppm (mixtures) } / \leq 10 \text{ ppm (pure gas)}$
H <sub>2</sub> O	$\leq 1 \text{ ppm (mixtures) } / \leq 10 \text{ ppm (pure gas)}$
O <sub>2</sub>	$\leq 1 \text{ ppm (mixtures) } / \leq 10 \text{ ppm (pure gas)}$
THC (CH <sub>4</sub> )	$\leq 1 \text{ ppm (mixtures) } / \leq 1 \text{ ppm (pure gas)}$
TFC (CF <sub>4</sub> )	$\leq 5 \text{ ppm (mixtures) } / \leq 5 \text{ ppm (pure gas)}$



***Our Xenon-129 gas mixtures are manufactured in accordance with cGMP regulations.***

# <sup>15</sup>Nitrogen - product information

## Nitrogen-15 in the form of gas and salts for medical and agricultural applications

Nitrogen-15 (<sup>15</sup>N) is mainly used for the synthesis of <sup>15</sup>N-labelled chemical compounds. These <sup>15</sup>N-labelled compounds are used for medical and biomedical applications as well as improving the harvest in agriculture.

In recent years, great progress has also been made in the hyperpolarization of small <sup>15</sup>N-labelled molecules, which can open up many new areas of research.

### Our Nitrogen-15 is available in the form of

- Nitrogen Gas
- Ammonium Chloride
- Ammonium Sulphate
- Potassium Nitrate
- Ammonium Nitrate
- Sodium Nitrate

Enrichment	<sup>15</sup> N ≥ 99at%
Purity	≥ 99.9%
Volume (gas)	Available in various volumes and various valve connections (please contact us).
Packing (salts)	400 g and/or 500 g bottles



# <sup>18</sup>Oxygen - product information

## Oxygen-18 in the form of water for medical applications

Oxygen-18 is used to synthesize radiopharmaceuticals labelled with Fluorine-18 (for example 2-fluoro-2-deoxy glucose [<sup>18</sup>FDG]). These are used for Positron Emission Tomography (PET), the most common cancer diagnostic technique.

**Our Oxygen-18 is available in the form of water**

Enrichment	$^{18}\text{O} \geq 98\text{at}\%$ , $^{17}\text{O} \leq 2\text{at}\%$ $^{16}\text{O} \leq 2\text{at}\%$
Purity	$\geq 99.9\%$
Volume	25 g & 50 g vials
Pyrogenicity	$< 0.25 \text{ EU/ml}$
Conductivity	$< 2 \mu\text{S/cm}$
pH	6 – 8



***Our Oxygen-18 products are manufactured in accordance with cGMP regulations and with the requirements of 21 Code of Federal Regulations: PARTS 210 and 211.***

## ISMRM-abstract about Oxygen-17 in the form of gas

### **Metabolic Brain Tumor Analysis: Correlation between ADC/ CBV and quantitative CMRO<sub>2</sub> employing dynamic <sup>17</sup>O MRI**

Sebastian C. Niesporek<sup>1</sup>, Nina Weinfurter<sup>2</sup>, Armin M. Nagel<sup>1,3</sup>, Mark E. Ladd, Heinz-Peter Schlemmer<sup>2</sup>, and Daniel Paech<sup>2</sup>

<sup>1</sup>Medical Physics in Radiology, German Cancer Research Center (DKFZ), Heidelberg, Germany, <sup>2</sup>Division of Radiology, German Cancer Research Center (DKFZ), Heidelberg, Germany, <sup>3</sup>Institute of Radiology, University Hospital Erlangen, Erlangen, Germany

**PURPOSE** Metabolic imaging is possible by employing dynamic <sup>17</sup>O-MRI [1] and is leading to robust and reproducible quantification of the cerebral metabolic rate of oxygen consumption (CMRO<sub>2</sub>) in volunteers [2] and patients [3]. The CMRO<sub>2</sub> parameter can be measured via dynamic <sup>17</sup>O-MRI of the stable oxygen isotope <sup>17</sup>O employing an inhalation procedure where enriched <sup>17</sup>O<sub>2</sub>-gas is administered during continuous imaging [1]. Recently, the first results of a first application in a brain tumor patient cohort [3] demonstrated the high specificity and metabolic contrast achievable: the whole tumor volume (TV, segmentation based on pure anatomical data) showed a significantly reduced CMRO<sub>2</sub> compared to healthy tissue. Dynamic methods often have the caveat that additional parameters like perfusion or cell density (e.g. in tumors) bias the true metabolic information. The presented work focusses on sub-compartment analysis of dynamic <sup>17</sup>O-MRI data in correlation between the apparent diffusion coefficient (ADC) and the cerebral blood volume (CBV) in high grade glioma patients.

**METHODS** Dynamic <sup>17</sup>O-MRI experiments were performed on a 7-Tesla-whole-body-scanner [4] with a nominal spatial resolution of (7.5mm)<sup>3</sup> employing a density-adapted radial sequence [5] with a Golden Angle acquisition scheme [6] (TR/TE=20/0.56ms, acquisition time t=30:00min) under administration of 3.8±0.1L of 70%-enriched <sup>17</sup>O<sub>2</sub>-gas [7]. The reconstructed temporal resolution was Δt = 1:00min. In total datasets of three WHO Grade IV were included. The workflow for partial volume (PV) correction of dynamic data was used as previously described [2,3] to obtain CMRO<sub>2</sub> information in TV and healthy tissue (normal appearing gray and white matter (NGM, NWM), CSF). Contrast-enhanced (CE) MPRAGE data (CE-T<sub>1w</sub>-MPRAGE, Fig.1A) were used for segmentation into masks of necrotic region (NE), contrast-enhancing region (CE) and peritumoral edema (PE) in n=3 patients. Additional information of clinical protocols (ADC/ CBV maps; Fig.1B, C) were coregistered to <sup>17</sup>O-data sets of dynamic inhalation experiments and used for a second and third segmentation entity (3D volume, ~20 slices). This classification based on ADC or CBV maps provided volumes of hyper- and hypo-intense volumes (CBV+/ADC-) for further, separate analysis of CMRO<sub>2</sub>. An analysis of variance (ANOVA) with Holm-Sidak pairwise comparisons was performed to test for statistically significant differences.

**RESULTS** All patient data in healthy tissue is showing a significantly increased CMRO<sub>2</sub> values in NGM compared to NWM (p<0.001). The quantitative evaluation yielded CMRO<sub>2,NGM</sub>=2.00–2.55±0.20μmol/g\*min compared to white matter tissue (CMRO<sub>2</sub>=0.72–0.92±0.09μmol/g\*min). Quantitative evaluation of healthy tissue and the tumor region of all patients is listed in Tab.1. Here one evaluation focused on CMRO<sub>2</sub> values in NE, CE and PE volumes; a second evaluation on CBV+ areal and a third evaluation on ADC- segmentation (NE-volume is always excluded from evaluation). Tumor metabolism is showing a significant functional decrease in the tumor tissue, with lowest values in NE as well as CE tumor region, compared to NGM or NWM (p<0.01). CBV analysis yields comparable metabolic information in CBV+ (strongly perfused) areas and no increased CMRO<sub>2</sub>. The same is observed in ADC- volumes where in both cases no significant change is seen to TV or CE evaluation (p>0.05). A complete overview is given in Fig.2. Maps of relative signal change with correlated anatomical information as well as segmentation outlines for all three segmentation approaches can be found in Fig.1.

**DISCUSSION** Dynamic <sup>17</sup>O-MRI is providing a specific metabolic contrast, seen in the significant drop in CMRO<sub>2</sub> values of malignant tissue. To exclude effects originating from cell density or varying blood perfusion an analysis based on CBV and ADC maps are connected to the metabolic information. A significantly reduced (p<0.01) CMRO<sub>2</sub> in CBV+ and ADC- regions to healthy tissue and comparable

values to evaluation based on CE-data demonstrates a perfusion and ADC independent information. Due to low spatial resolution and rapid transverse relaxation, the dynamic quantitative  $^{17}\text{O}$ -signal might be underestimated despite the application of a dedicated PVC algorithm. As discussed in previous studies [2] the main sources of error are the uncertainty in the prior  $^{17}\text{O}$ -enrichment and limitations of the PVC. However, quantified metabolic information in NGM and NWM are in good agreement with previous work [1,2]. For better statistical evaluation a larger number of examinations would be desirable, but nevertheless the first results and number of patients provide sufficient information to assess ADC and CBV correlation in a first trial.

**CONCLUSION** This study presents data of the first examined patient cohort of dynamic  $^{17}\text{O}$ -MRI in a sub-compartment analyses focusing on ADC and CBV correlation. Results support the hypothesis that this method provides a very specific and pure metabolic information independent of tissue perfusion and cellular density. Increasing of total patient number, a correlation to other modalities, e.g. PET could establish  $^{17}\text{O}$ -MRI as a tool to provide further insight into tumor pathophysiology beyond anatomical borders.

**REFERENCES** [1] Atkinson IC, Neuroimage 2010 (51):723-733; [2] Niesporek, SC, Magn Reson Med 2018; 79: 2923–2934; [3] Niesporek SC, In Proc. ISMRM 2018, #625; [4] Siemens Healthineers, Erlangen, Germany; [5] Nagel et al., Magn Reson Med 2009 (62):1565-73; [6] Chan, R.W. et al., Magn Reson Med 2009(61): p. 354–363; [7] NUKEM Isotopes Imaging GmbH, Alzenau, Germany.

**ACKNOWLEDGMENT** The authors want to thank NUKEM Isotopes Imaging GmbH for their generous supply of  $^{17}\text{O}_2$ -gas and support of this project.

**Alternative title:**

*“Dynamic  $^{17}\text{O}$  MRI in human brain tumors is independent of perfusion and ADC”*

**Tab.1** Complete results of CMRO<sub>2</sub> quantification in tumor and healthy tissue. Dynamic  $^{17}\text{O}$  data is evaluated in healthy tissue (normal gray matter (NGM), normal white matter (NWM)) and in tumor segmentation. Three separate evaluations were conducted based on three different manual segmentations: 1) tumor volume and contrast enhancement based on contrast enhanced T<sub>1w</sub>-MPRAGE (CE-T<sub>1w</sub>-MPRAGE); 2) CBV+: CBV hyper-intense map volume based on CBV data; 3) ADC-: ADC hypo-intense map based on ADC data.

CMRO <sub>2</sub> in $\mu\text{mol}/(\text{g min})$						
Patient	Tumor segmentation (CE-T <sub>1w</sub> -MPRAGE, CBV, ADC)				Healthy tissue	
	Tumor volume (TV)	contrast enhancement (CE)	CBV+	ADC-	NGM	NWM
#2	0.22±0.08	0.21±0.08	0.20±0.05	0.11±0.05	2.55±0.12	0.72±0.05
#3	0.18±0.07	0.25±0.10	0.26±0.08	0.10±0.09	2.00±0.12	0.85±0.08
#6	0.33±0.06	0.35±0.12	0.37±0.06	0.30±0.08	2.43±0.15	0.92±0.05

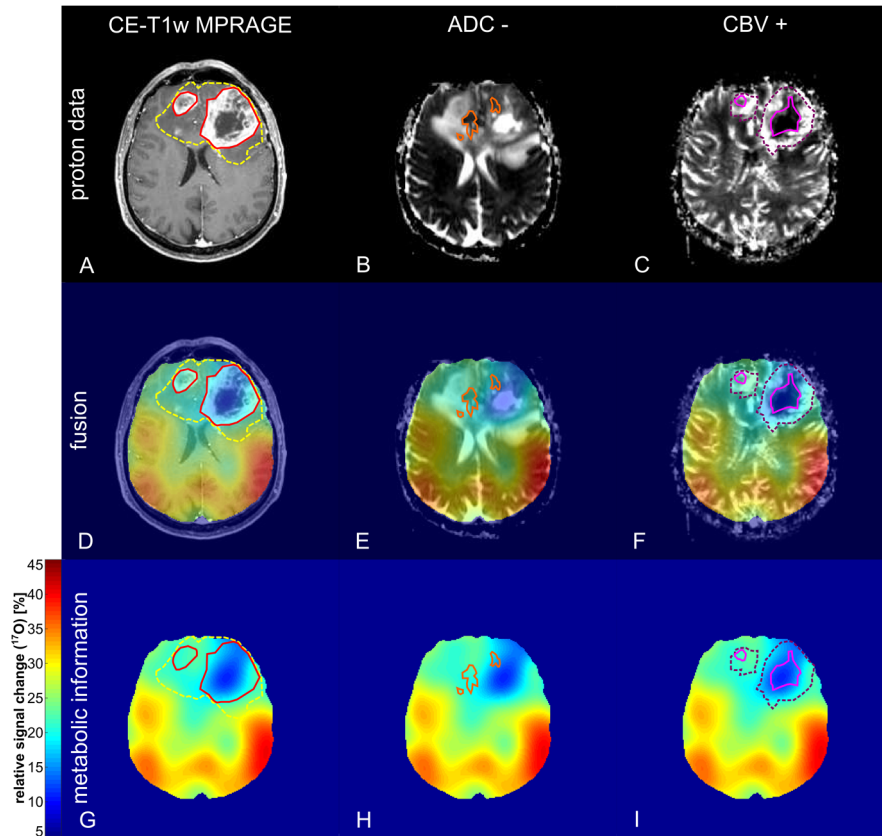


**Fig.1** Proton and dynamic  $^{17}\text{O}$  MRI data with corresponding segmentation. Three segmentation masks of the tumor volume were utilized in  $\text{CMRO}_2$  quantification: CE-T1w-MPRAGE, CBV, ADC (A-C). Outlines of segmentation masks are shown in fusion (D-F) with maps of relative signal change of  $^{17}\text{O}$  signal in the course of the inhalation experiment (G-I). Segmentation masks outlines show the contrast enhancement and peritumoral edema (red/ yellow; A,D,G), ADC-: ADC hypo-intense volume (orange, B,E,H) as well as CBV+: CBV hyper-intense and necrotic area (red/ purple, C,F,I). A clear depressed signal increase (5-15%) is observable indicating a corresponding change of  $\text{CMRO}_2$ .

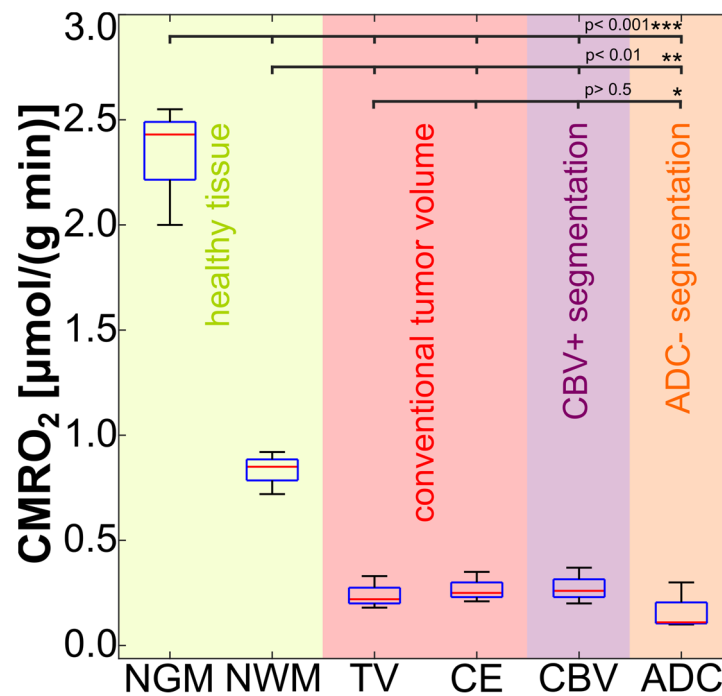


**Fig.2** Overview of sub-compartment analysis based on three different tumor evaluation methods (CE-T1w-MPRAGE, CBV, ADC) for all three patients. All considered tumor volume segmentations are showing a significantly reduced  $\text{CMRO}_2$  ( $p < 0.01$ ) compared to healthy tissue. Evaluation based on CBV and ADC segmentation (CBV+/ ADC-) are not showing a significantly increased  $\text{CMRO}_2$  compared to conventional tumor segmentation based on CE-T1w-MPRAGE (tumor volume (TV), contrast enhancement (CE)).

# Protocol Optimization for Functional $^{17}\text{O}$ -MRI of Donor Kidneys at 3T

Yanis Taege<sup>1</sup>, Johannes Fischer<sup>1</sup>, Ali Çağlar Özen<sup>1,2</sup>, Hao Song<sup>1</sup>, Christian Schuch<sup>3</sup>, Rianne Schutter<sup>4</sup>, Cyril Moers<sup>4</sup>, Ronald JH Borra<sup>5</sup>, and Michael Bock<sup>1</sup>

<sup>1</sup>Department of Radiology, Medical Physics, Medical Center - University of Freiburg, Faculty of Medicine, University of Freiburg, Freiburg, Germany,

<sup>2</sup>German Cancer Consortium Partner Site Freiburg, German Cancer Research Center (DKFZ), Heidelberg, Germany,

<sup>3</sup>NUKEM Isotopes Imaging GmbH, Alzenau, Germany,

<sup>4</sup>Department of Surgery – Organ Donation and Transplantation, University Medical Center Groningen, Groningen, Netherlands,

<sup>5</sup>Medical Imaging Center, University Medical Center Groningen, Groningen, Netherlands

**SYNOPSIS** Direct  $^{17}\text{O}$ -MRI is able to measure the dynamics of renal metabolism in a porcine kidney in an organ transplantation setup at 3T. To obtain stable SNRs above 20 over time while maintaining a spatial resolution below 8 mm, we investigated the influence of nominal spatial resolution, bandwidth and acquisition time window of a UTE-sequence with a golden-angle acquisition pattern on SNR. Signal increase of up to 25% per liter of  $^{17}\text{O}$ -gas was observed in a pilot experiment.

**INTRODUCTION** Most organ transplants are renal transplants<sup>1–3</sup>, but even though biomarkers exist to diagnose complications after kidney transplantation<sup>4</sup>, survival rates decrease drastically with the time after transplantation<sup>5,6</sup>. One reason for post-transplantation complications is the insufficient functional characterization of the transplanted kidney. It would thus be advantageous to measure renal function in vitro to quantify the suitability of a resected kidney before implantation. Besides perfusion and renal filtration, an important renal function parameter is tissue oxygenation.

A direct method to assess the metabolic rate of oxygen consumption is dynamic  $^{17}\text{O}$ -MRI, which has been extensively used for metabolic measurements in the brain<sup>7–14</sup>. In this work, we propose and optimize a  $^{17}\text{O}$ -MR measurement protocol to spatially assess renal metabolic rates of oxygen consumption in donor organs before transplantation.

**MATERIALS AND METHODS** To perform robust mapping of the renal metabolic rate of oxygen consumption ( $\text{RMRO}_2$ ) with  $^{17}\text{O}$ -MRI, the acquisition parameters need to be optimized to achieve a nominal spatial resolution of  $\Delta x = 6\text{mm}$ , a minimal temporal resolution of  $\Delta t = 2\text{ min}$  while maintaining a  $\text{SNR} > 20$ .

## Protocol Optimization

$^{17}\text{O}$ -MRI protocol optimization was performed at a clinical 3T MR system (Prisma FIT; SIEMENS, Erlangen, Germany) with a custom-built Tx/Rx  $^{17}\text{O}$ -head coil. For image acquisition a radial UTE sequence with golden-angle (GA) projection acquisition pattern<sup>16</sup> was used. The acquired spokes were divided using a sliding window reconstruction technique such that each image covers a specified reconstruction time window  $\Delta t_w$ . Kaiser-Bessel-regridding<sup>17</sup> of k-space data and Hanning-filtering was subsequently applied in each frame. SNR was optimized as a function of  $\Delta x$ , BW and  $\Delta t_w$ , and other imaging parameters (Tab. 1) were taken from previous  $\text{CMRO}_2$  experiments in human brain<sup>7</sup>.

We numerically investigated the influence of the readout BW on the full-width-half-maximum (FWHM) of the point-spread-function by simulating the  $T_2^*$ -decay ( $T_2^* = 1.8\text{ms}$ )<sup>18</sup> during the acquisition with the given parameters and resulting gradient shapes. The influence of different combinations of BW and  $\Delta x$  was experimentally evaluated on a homogeneous phantom with slightly larger dimensions than a kidney<sup>19</sup> ( $\text{vol} = 450\text{mL}$ ) filled with 0.9% NaCl. To scale the SNR dependency with the acquisition time, a non-linear fit  $\text{SNR} = A \cdot \sqrt{(\Delta t_w)}$  was applied<sup>20</sup>.

To demonstrate that the optimized protocol is suitable for dynamic  $^{17}\text{O}$ -MRI, images of a oxygenated porcine kidney were acquired at a clinical 3T MR system (Prisma; SIEMENS, Erlangen, Germany) with a custom-built Tx/Rx  $^{17}\text{O}$ -loop coil using our optimized parameters (Tab. 1).

**RESULTS** All combinations of BW and  $\Delta x$  of the SNR dependency on  $\Delta t_w$  showed the expected dependency on the square-root of time (Fig. 1,  $R^2 > 0.9$ ), and A decreased with BW and increased with  $\Delta x$  (Fig. 2a). The simulation of the PSF (Fig. 2b) revealed a decrease of FWHM-factors with increasing bandwidth, approaching a limit of 2.2. For the lowest possible BW of 200 Hz/px in the desired parameter combinations, a FWHM-factor of 2.75 was found, while factors of below 2.5 were accomplished at BWs below 300 Hz/px. Figure 3 shows the anatomical  $^1\text{H}$ -MPRAGE image obtained with the body coil next to the interpolated  $^{17}\text{O}$ -magnitude signal averaged over the entire acquisition time. The mean kidney  $^{17}\text{O}$ -signal dynamically increased during  $^{17}\text{O}$ -oxygenation by up to 20% and remained relatively stable during the remaining time (Fig. 4).

**DISCUSSION** In the desired parameter range ( $\text{SNR} > 20$ ,  $\Delta t \leq 120$ ), a spatial resolution of 6 mm could be achieved while maintaining a BW below 400 Hz/px. Although a BW of 200 Hz/px at 6mm resolution would result in the highest SNR values for the lowest possible nominal resolution, the associated blurring (FWHM-factor 2.75) would deteriorate the spatial accuracy of the measurement. Thus,  $\Delta x$  and BW were set to 6 mm and 280 Hz/pixel (Tab. 1), respectively, such that images could be reconstructed with an acquisition time down to 90s while maintaining the FWHM-factor in the range of 2.5. In the pilot experiment dynamic  $^{17}\text{O}$ -signals could be acquired over a time course of 72 minutes from a porcine kidney with SNR values above 20 in the ROI. The signal increase in the area of the kidney was similar those of previous  $\text{CMRO}_2$  experiments in brain, which were in the range of 10-35%<sup>7-9,14</sup>.

**CONCLUSIONS** Parameter optimization of functional  $^{17}\text{O}$ -MRI in transplants as small as kidneys at 3T is a challenging compromise between low bandwidths and nominal resolution. Nevertheless, we were able to perform a proof-of-concept experiment with the concluded parameters, which shows the possibility of dynamic  $^{17}\text{O}$ -MRI with SNRs above 20 and a temporal resolution down to 90 s. Due to direct oxygenation of the organ, the efficiency of used  $^{17}\text{O}_2$  of 25%/L is higher than those of previous  $\text{CMRO}_2$  experiments of 2.5-10%/L.

**ACKNOWLEDGEMENTS** Support from NUKEM Isotopes Imaging GmbH is gratefully acknowledged.

## REFERENCES

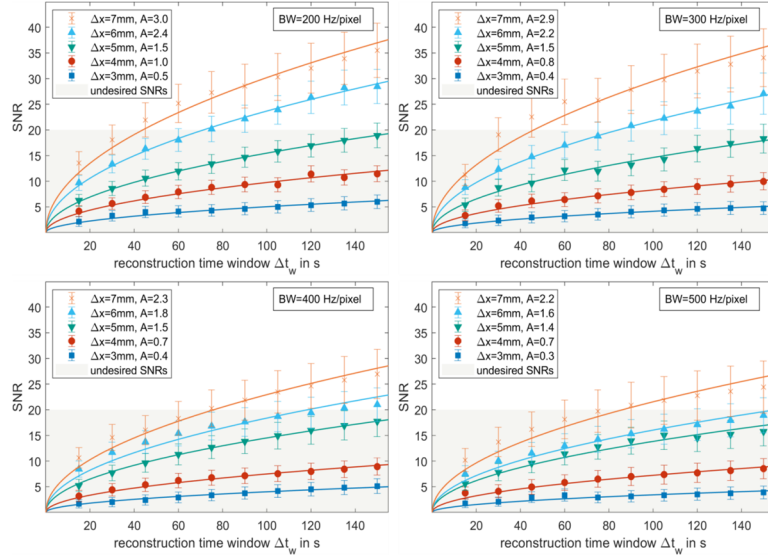
1. Branger, P. & Samuel, U. Annual Report 2017. 124 (Eurotransplant International Foundation, 2017).
2. Hart, A. et al. OPTN/SRTR 2016 Annual Data Report: Kidney. Am. J. Transplant. 18, 97
3. Department of Health and Human Services, Health Resources and Services Administration, Healthcare Systems Bureau, Division of Transplantation. Annual Report of the U.S. Organ Procurement and Transplantation Network and the Scientific Registry of Transplant Recipients: UNOS (2016). Available at: <https://unos.org/about/annual-report/2016-annual-report/>. (Accessed: 30th October 2018)
4. Salvadori, M. & Tsalouchos, A. Biomarkers in renal transplantation: An updated review. World J. Transplant. 7, 161–178 (2017).
5. Pestana, J. M. Clinical outcomes of 11,436 kidney transplants performed in a single center - Hospital do Rim. J. Bras. Nefrol. 39, (2017).
6. Wang, J. H., Skeans, M. A. & Israni, A. K. Current Status of Kidney Transplant Outcomes: Dying to Survive. Adv. Chronic Kidney Dis. 23, 281–286 (2016).
7. Kurzhunov, D. et al. 3D  $\text{CMRO}_2$  mapping in human brain with direct  $^{17}\text{O}$  MRI: Comparison of conventional and proton-constrained reconstructions. NeuroImage 155, 612–624 (2017).
8. Kurzhunov, D., Borowiak, R., Reisert, M., Özen, A. C. & Bock, M. Direct estimation of  $^{17}\text{O}$  MR images (DIESIS) for quantification of oxygen metabolism in the human brain with partial volume correction. Magn. Reson. Med. (2018). doi:10.1002/mrm.27224
9. Niesporek, S. C. et al. Reproducibility of  $\text{CMRO}_2$  determination using dynamic  $^{17}\text{O}$  MRI: Direct  $\text{CMRO}_2$  Measurements: Reproducibility Study. Magn. Reson. Med. 79, 2923–2934 (2018).

10. Liu, Y. et al. High-resolution dynamic oxygen-17 MR imaging of mouse brain with golden-ratio-based radial sampling and k-space-weighted image reconstruction: Dynamic  $^{17}\text{O}$ -MRI of Mouse Brain. *Magn. Reson. Med.* 79, 256–263 (2018).
11. Zhu, X.-H. & Chen, W. In vivo  $^{17}\text{O}$  MRS imaging – Quantitative assessment of regional oxygen consumption and perfusion rates in living brain. *Anal. Biochem.* 529, 171–178 (2017).
12. Zhu, X.-H., Zhang, Y., Wiesner, H. M., Ugurbil, K. & Chen, W. In vivo measurement of CBF using  $^{17}\text{O}$  NMR signal of metabolically produced  $\text{H}_2^{17}\text{O}$  as a perfusion tracer: Simultaneous CBF and  $\text{CMRO}_2$  Measurement. *Magn. Reson. Med.* 70, 309–314 (2013).
13. Zhu, X.-H., Chen, J. M., Tu, T.-W., Chen, W. & Song, S.-K. Simultaneous and noninvasive imaging of cerebral oxygen metabolic rate, blood flow and oxygen extraction fraction in stroke mice. *NeuroImage* 64, 437–447 (2013).
14. Hoffmann, S. H., Radbruch, A., Bock, M., Semmler, W. & Nagel, A. M. Direct  $^{17}\text{O}$  MRI with partial volume correction: first experiences in a glioblastoma patient. *Magn. Reson. Mater. Phys. Biol. Med.* 27, 579–587 (2014).
16. Chan, R. W., Ramsay, E. A., Cunningham, C. H. & Plewes, D. B. Temporal stability of adaptive 3D radial MRI using multidimensional golden means. *Magn. Reson. Med.* 61, 354–363 (2009).
17. Jackson, J. I., Meyer, C. H., Nishimura, D. G. & Macovski, A. Selection of a convolution function for Fourier inversion using gridding (computerised tomography application). *IEEE Trans. Med. Imaging* 10, 473–478 (1991).
18. Zhu, X.-H., Merkle, H., Kwag, J.-H., Ugurbil, K. & Chen, W.  $^{17}\text{O}$  relaxation time and NMR sensitivity of cerebral water and their field dependence. *Magn. Reson. Med.* 45, 543–549 (2001).
19. Cheong, B., Muthupillai, R., Rubin, M. F. & Flamm, S. D. Normal Values for Renal Length and Volume as Measured by Magnetic Resonance Imaging. *Clin. J. Am. Soc. Nephrol.* 2, 38–45 (2006).
20. Brown, R. W., Cheng, Y.-C. N., Haacke, E. M., Thompson, M. R. & Venkatesan, R. Magnetic resonance imaging: physical principles and sequence design. (John Wiley & Sons, Inc, 2014).

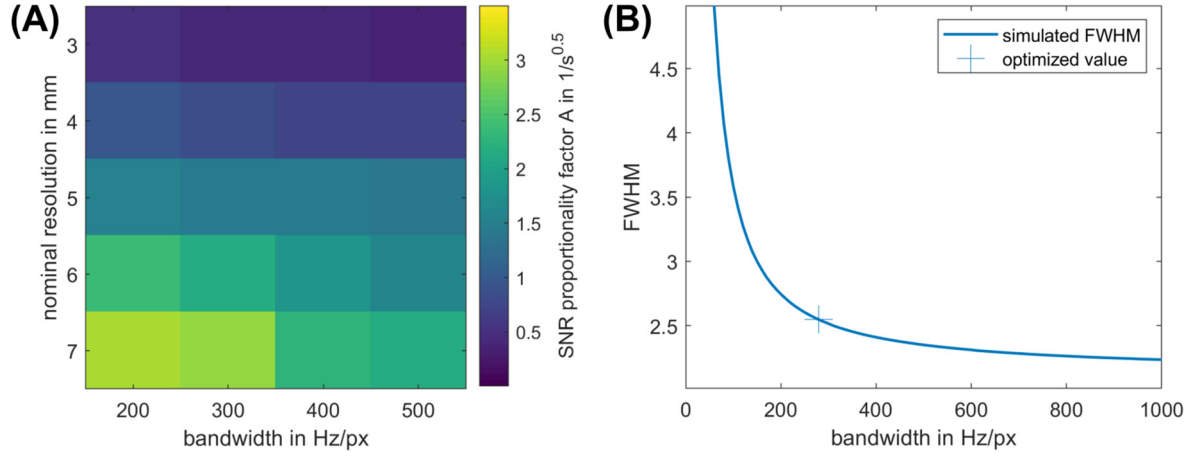
## FIGURES

Table 1: Sequence parameter overview of the optimization process and the experiment.  $\Delta x$  denotes the nominal spatial resolution, TRF the length of the RF pulse,  $\Delta t_w$  the length of the acquisition time window,  $\Delta t$  the temporal resolution,  $N_{\text{Spokes}}$  the total number of spokes acquired per measurement, BR the base resolution and OS the oversampling factor.

Value unit	TE ms	TR ms	Bandwidth Hz/pixel	$\Delta x$ mm	$T_{\text{RF}}$ ms	$\Delta t_w$ s	$\Delta t$ s	$N_{\text{Spokes}}$ -	BR	OS
optimization	0.56	12	[200 – 500]	[3 – 7]	1.0	[15 – 150]	n/a	13'500	32	2
experiment	0.56	12	280	6	1.0	120	60	375'000	32	2



**Figure 1:** SNR dependency on reconstruction time window  $\Delta t_w$  for different bandwidths and nominal resolutions  $\Delta x$ . Undesired values of SNR below 20 are denoted by the shaded gray area. Since the acquisition time is proportional to the number of spokes, the relation  $\text{SNR} = A \cdot \sqrt{\Delta t_w}$ , was fitted ( $R^2 > 0.9$ ), with  $A$  being the proportionality factor of the SNR in  $\sqrt{s}$ . An overview over values of  $A$  is given in Figure 2.



**Figure 2:** Overview of the results of the protocol optimization. (A) Overview over the dependency of the SNR proportionality factor  $A$  (Fig. 1) on nominal resolution and bandwidth. (B) Simulation results showing the FWHM dependency of the point-spread-function (PSF) on bandwidth (BW).

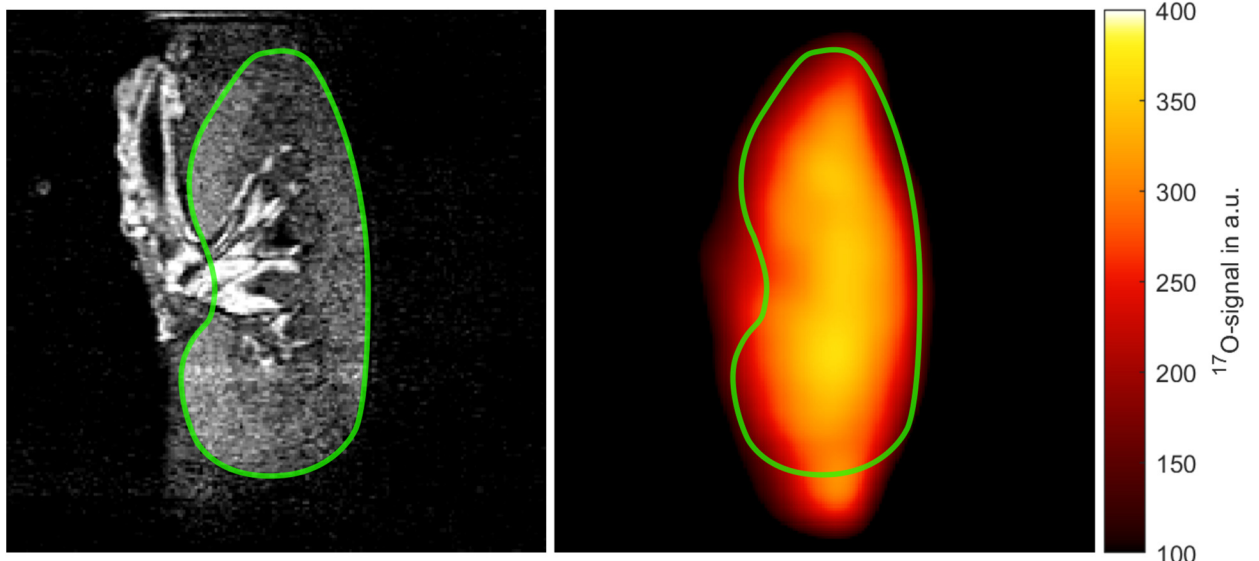


**Figure 3:** Anatomical, isotropic  $^1\text{H}$ -MPRAGE image of the perfused porcine kidney (left) and the corresponding interpolated  $^{17}\text{O}$ -magnitude data (right), which were averaged over the entire scan time. Both images are intrinsically registered since H-data were acquired with the body coil while the  $^{17}\text{O}$ -coil was inserted.

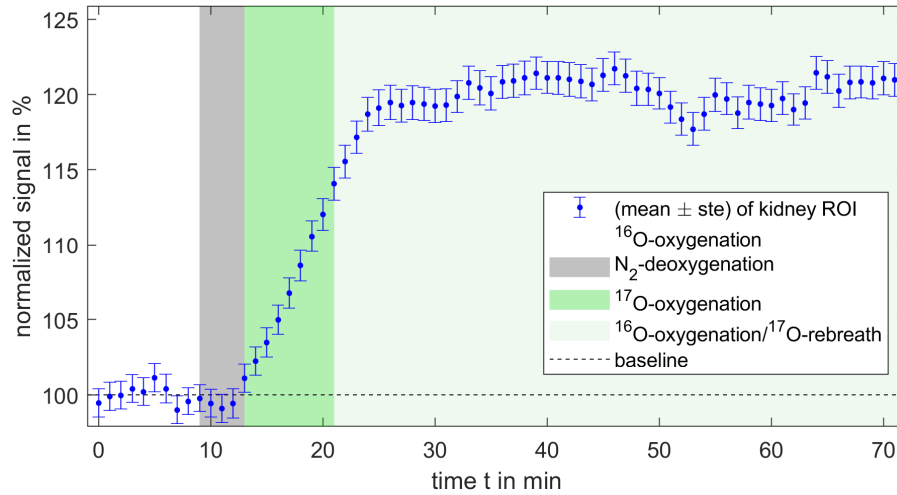


**Figure 4:** Results of the dynamic  $^{17}\text{O}$ -perfusion experiment in a porcine kidney. Shown are the mean values of the kidney's  $^{17}\text{O}$ -signal, normalized to the mean of the first 10 minutes of the scan. Error bars denote the standard error of the mean over the 2min of acquisition time. The green, shaded area marks the time period in which 0.8L of 70%-enriched  $^{17}\text{O}_2$ -gas (NUKEM Isotopes Imaging, Alzenau, Germany) were administered.

## A PET COMPATIBLE $^{17}\text{O}/^1\text{H}$ COIL FOR SIMULTANEOUS MULTINUCLEAR PET/MR

Karthik Lakshmanan<sup>1</sup>, Seena Dehkharghani<sup>1</sup>, Guillaume Madelin<sup>1</sup>, and Ryan Brown<sup>1</sup>

<sup>1</sup>NYU School of Medicine, New York, NY, United States

**SYNOPSIS** Direct MR oximetry by imaging  $^{17}\text{O}$  isotope can be a viable alternative over the conventionally used  $^{15}\text{O}$  PET tracer. In this work we developed a dual-tuned  $^{17}\text{O}/^1\text{H}$  coil array with potential PET compatibility to explore brain oximetry and support simultaneous PET tracers to provide complementary insights into brain function.

**INTRODUCTION** Brain homeostasis depends critically upon the steady nutritive flow of oxygenated blood, hinging on the immense energetic advantage of oxidative phosphorylation to sustain the neurovascular unit at rest and during explicit activation. Seminal paradigms describing hemodynamic compromise amid declining perfusion pressures were expounded through use of  $^{15}\text{O}$  PET, emphasizing a tenuous state of misery perfusion marked by impaired oxygen metabolism and conferring elevated near-term stroke risk<sup>1-3</sup>. Technical obstacles associated with  $^{15}\text{O}$  have motivated the exploration of direct MR oximetry, exploiting the stable and naturally occurring  $^{17}\text{O}$  isotope as an alternative to assess oxygen metabolism. However, its low natural abundance (0.037%) has demanded ultrahigh field imaging conditions coupled to fractionally enriched  $^{17}\text{O}$  gas inhalation, limiting widespread translational or clinical applicability<sup>4-7</sup>. In this work we developed a dual-tuned  $^{17}\text{O}/^1\text{H}$  coil array with potential PET compatibility to explore the feasibility of natural abundance high sensitivity brain oximetry at 3T and supporting simultaneous PET tracers and molecular imaging providing complementary insights into brain metabolism.

**METHODS** Design Approach: To achieve optimal multinuclear performance we engineered a coplanar interleaved coil<sup>8</sup> comprised of two radially interleaved degenerate mode birdcage structures with four ( $^{17}\text{O}$ , 16.7 MHz) and eight ( $^1\text{H}$ , 123.2MHz) channels (Fig.1, 2). To minimize PET attenuation, we consolidated the arrays into a two "layer" structure, moved the interface components and majority of tuning capacitors outside the PET FOV, and enclosed the device in a 3D printed (Fortus 360, Stratasys) stealth polycarbonate shell.

**$^{17}\text{O}$  Array:** The  $^{17}\text{O}$  unit is a transmit/receive array with 4 elements (27 cm long (H-F) and 30 cm arc length). The neighboring elements were decoupled by geometrical overlap and the next nearest neighbors by linked inductors. The  $^{17}\text{O}$  array was driven in CP mode (using a 1:4 way power-divider and phase shifters) during transmission to achieve spin excitation; during signal reception the coil operated as a phased array to maximize SNR.

**<sup>1</sup>H Array:** The <sup>1</sup>H unit is a receive only phased array with 8 elements (24 cm long and 12 cm arc length). The neighboring elements were decoupled by capacitors in the shared rungs. One active detuning circuit and one current fuse (700 mA) were implemented per <sup>1</sup>H element to ensure patient safety and to isolate the array during body coil transmission, which was favored due to its large excitation coverage for applications such as spin labeling.

**Trap Circuits:** The perimeter of the oxygen loops is 114 cm, long enough to support standing waves at 123.2MHz. To ensure patient safety during body coil excitation, two <sup>1</sup>H trap circuits were incorporated per <sup>17</sup>O element.

**Imaging:** Phantom and in vivo measurements were performed using a whole-body 3T scanner (Prisma, Siemens Healthineers, Germany) upon approval by our local IRB and informed written consent from the participants. <sup>17</sup>O images were acquired using a FLORET9 sequence. The <sup>1</sup>H performance was compared against a standard clinical head array (Siemens). <sup>1</sup>H B + and SNR maps were derived from TurboFLASH<sup>10</sup> and GRE acquisitions both with and without RF excitation on head shaped gel phantom whose dielectric properties matched those of the brain<sup>11</sup>.

**RESULTS - BENCH MEASUREMENTS** <sup>17</sup>O: Unloaded and loaded Q of the <sup>17</sup>O elements were 250 and 100 with a ratio of 2.5. <sup>17</sup>O elements were tuned and matched to 50Ω at 16.7MHz with an average reflection of -15dB. Average isolation was -14 and -18dB between neighbors and next nearest neighbors respectively.

<sup>1</sup>H: Unloaded and loaded Q of the <sup>1</sup>H elements were 310 and 85 with a ratio of 3.6. <sup>1</sup>H elements were tuned and matched to 50Ω at 123.2MHz with an average reflection of -15dB. Average isolation was -9 and -11dB between neighbors and next nearest neighbors respectively.

**IMAGING** <sup>17</sup>O: Excitation efficiency was characterized by achieving a 90° flip angle with a 500μs hard pulse with 240v amplitude. <sup>17</sup>O in vivo images (Fig.3) confirm the feasibility of natural abundance MR oximetry at 3T using the <sup>17</sup>O/<sup>1</sup>H coil array.

<sup>1</sup>H: In phantom experiments achieving a 90° flip angle with a 500μs hard pulse required 202v. <sup>1</sup>H B + maps (Fig.4) show that the <sup>17</sup>O/<sup>1</sup>H array caused minimal distortion to the body coil transmit field. SNR maps (Fig.5) show that at the center of the phantom the 20 channel array outperforms the <sup>17</sup>O/<sup>1</sup>H array approximately by 20%. 1mm isotropic MPAGE images (Fig.6) show that the <sup>17</sup>O/<sup>1</sup>H provides adequate uniformity, coverage and SNR.

**CONCLUSIONS AND DISCUSSION** Derangements in oxygen metabolism are fundamental to many pathologic processes. We developed a dual-tuned <sup>17</sup>O/<sup>1</sup>H coil for simultaneous PET/MR on a clinical 3T system. Despite the use of high impedance trap circuits on the <sup>17</sup>O elements, the <sup>17</sup>O performance was not compromised. Our coil array can potentially facilitate simultaneous <sup>17</sup>O-MRI functional issue characterization and PET neuroimaging.

**ACKNOWLEDGEMENTS** The authors thank Jerzy Walczysk for his efforts on the coil housings.

## FIGURES

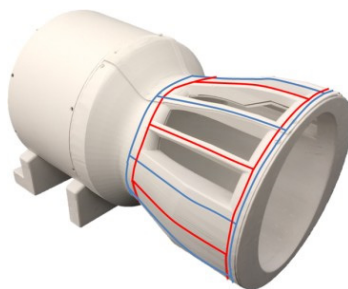


**Figure 1.** Coil Image. <sup>17</sup>O- 4 elements, blue. During <sup>17</sup>O transmit the coil array works in CP mode (using a 1:4 way power divider and phase shifters). During receive the coil works as a phased array. <sup>1</sup>H - 8 elements, red. The <sup>1</sup>H elements are received only and the coil operates in phased array mode.

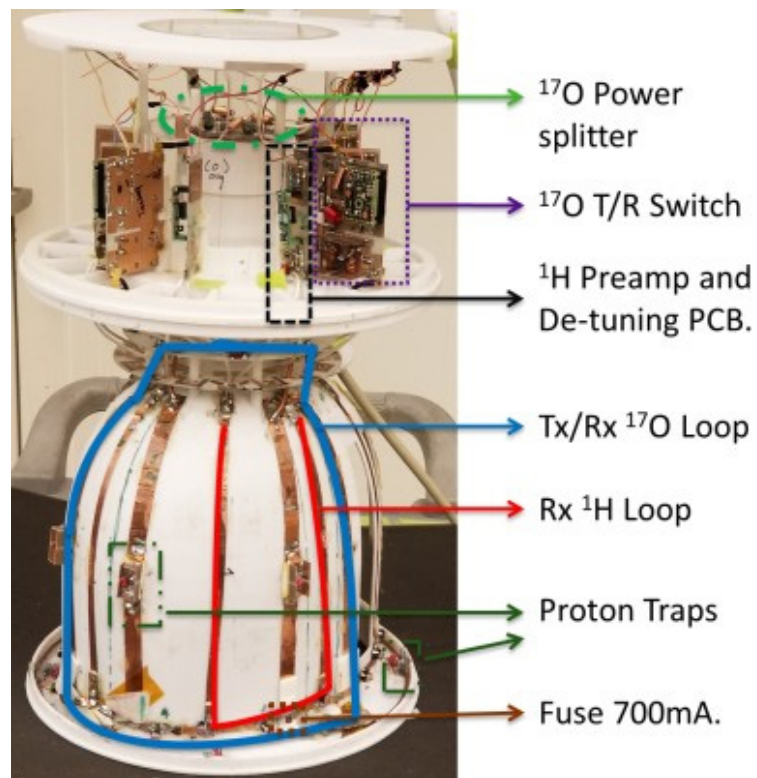


Figure 2. Coil layout with major assemblies identified and labeled.

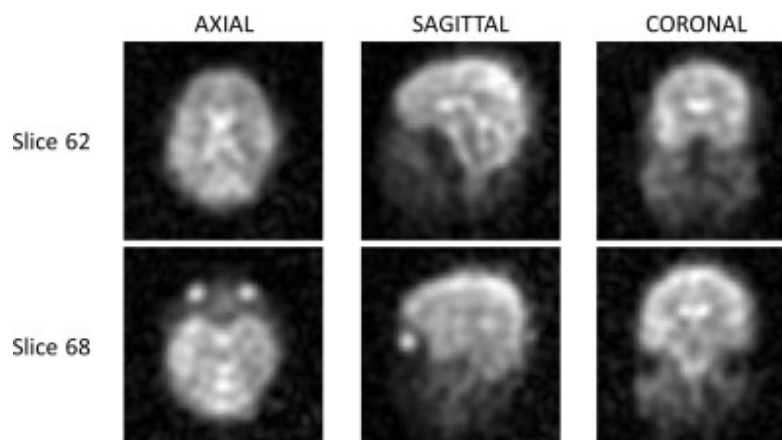
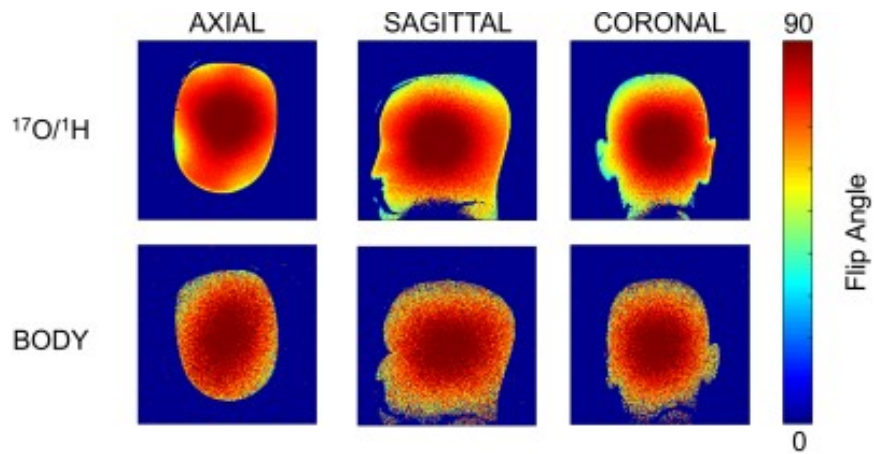
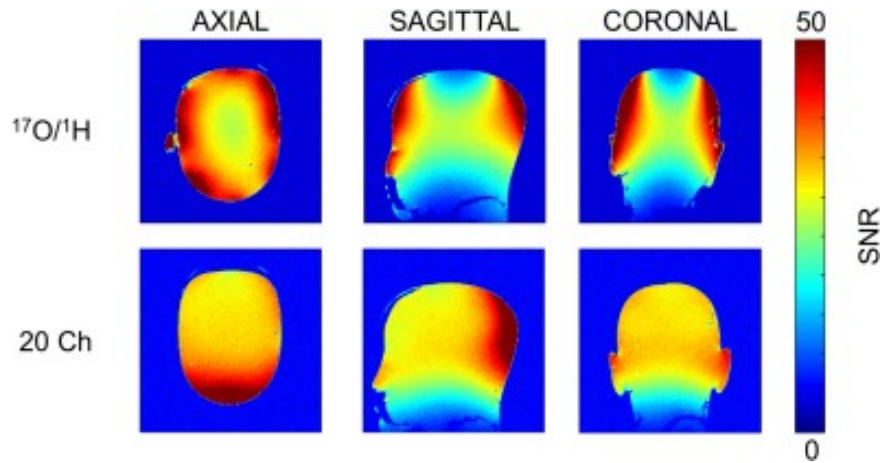


Figure 3.  $^{17}\text{O}$  brain Images in different slices of a 3D FLORET acquisition (TE/TR 0.2/50 ms, FoV 512 mm, Matrix 64x64x64, Resolution 8 mm isotropic, 3 hubs at 45 deg. 140 interleaves per hub, FA 90°, Pulse duration 0.5ms, 56 averages, readout time 0.3 ms, acquisition time 19:30 min)



**Figure 4.**  $^1\text{H}$  TFL B + maps (TR/FA 10000/  $10^\circ$  on a GEL Head Phantom) acquired with and without the  $^{17}\text{O}/^1\text{H}$  Array. The flip angle maps show that the presence of the  $^{17}\text{O}/^1\text{H}$  array causes minimal distortion to the body coil transmit field indicating adequate current suppression was provided by the  $^1\text{H}$  trap circuits.



**Figure 5.**  $^1\text{H}$  SNR Maps. GRE Sequence (TR/TE/FLIP/BW/Slice 500 ms/3.82 ms/ $10^\circ$ /260 Hz/3 mm, Matrix 256, FoV 250 mm).



**Figure 6.**  $^1\text{H}$  MPRAGE Images. (TR/TE/TI/FLIP 2200 ms /3.2 ms/900 ms/9, Resolution 1 mm isotropic, acceleration factor 2, acquisition time 4:30 min).

## **SMRM-abstract ( $^{17}\text{O}$ in the form of D-Glucose)**

### **Limitation of glucose consumption in rat head detected by labeled glucose- $^{17}\text{O}$**

Victor D. Schepkin<sup>1</sup>, Shannon Helsper<sup>1</sup>, and Cathy Levenson<sup>2</sup>

<sup>1</sup>Florida State University/NHMFL, Tallahassee, FL, United States, <sup>2</sup>MSR, Florida State University/NHMFL, Tallahassee, FL, United States

**SYNOPSIS** In animal experiments using  $^{17}\text{O}$  labeled glucose, questions arose regarding the relatively stable rate of glucose metabolism, compared with a simultaneous variation in glucose concentration after bolus injection. Bolus Glucose-6- $^{17}\text{O}$  administration with doses 3-15  $\mu\text{mol/g}$  for normal rats revealed the same glucose consumption with  $\text{CMR}_{\text{glc}} = 0.43 \pm 0.06 \mu\text{mol/g tissue/min}$ . After bolus injection, the rate of glucose metabolism was consistent in each dose regardless of the large variation in glucose concentration. The results correlate with the observations of others, indicating that glucose-6-phosphate (G-6-P) does not accumulate in hyperglycemia and can limit glucose consumption.

**INTRODUCTION** Glucose metabolism has a major role in energy metabolism in vivo. The rate of glucose metabolism can be determined by oxygen or glucose consumption. For example, one can have both components labeled by  $^{17}\text{O}$  nuclei, which is suitable for MR detection. Either approach examines the same reaction of glucose metabolism, but from different points of view and provides different information, which exceeds the well-known metabolic association between oxygen and glucose 1. In animal experiments using  $^{17}\text{O}$  labeled glucose, questions arose regarding the relatively stable rate of glucose metabolism over an hour during simultaneous variation in glucose concentration after bolus injection. This contrasting situation was observed in a mouse brain 2 with a glucose injection dose of 13.8  $\mu\text{mol/g}$ . In the current study, experiments with rats were conducted using a range of doses for injected glucose to confirm and analyze such observations.

**METHODS** Intravenous tail administrations of glucose-6- $^{17}\text{O}$  (abundance 38-47%) were investigated by detecting  $^{17}\text{O}$  MR signal from a rat head at 21.1 T. The MR experiments were performed using Bruker MRI Avance III console (PV 5.1 software). The in vivo RF probe has a double tuned  $^{17}\text{O}/^1\text{H}$  volume RF coil with an internal diameter of 33 mm, covering the whole rat head. The MR frequency for  $^{17}\text{O}$  was 121.65 MHz. The time course of the MR  $^{17}\text{O}$  signal changes was detected using 90 degree RF pulse of 160  $\mu\text{s}$ , TR time of 90 ms and NA = 166; thus, the time course resolution was 15 s/point. The MR signal allowed us to follow the changes of  $^{17}\text{O}$  labeled glucose and  $^{17}\text{O}$  metabolized water content at the same time. The injection of 1.5 mL PBS solution containing D-glucose-6- $^{17}\text{O}$  in the rat tail had duration of 1.5 min. Glucose injection doses were in the range of 3 - 15  $\mu\text{mol/g}$  of animal weight. The in vivo experiments were performed using 6 male Fisher 344 rats (~ 200 g) anesthetized by isoflurane 1.5%. All animal experiments were conducted according to the protocols approved by The Florida State University ACUC.

**RESULTS AND DISCUSSION** Experiments with glucose-6- $^{17}\text{O}$  labeled glucose were conducted allowing measurements of glucose consumption without prior determination of CBF 3. Glucose consumption was determined by changes of the  $^{17}\text{O}$ -water signal. The same MR experiments permitted monitoring changes in the concentration of glucose through direct observation of the glucose-6- $^{17}\text{O}$  MR signal peak positioned separately at -12.3 ppm relative to the  $^{17}\text{O}$  water peak. The direct detection of glucose- $^{17}\text{O}$  in rat head demonstrates a large change of glucose concentration during the first hour after the bolus injection (Fig. 1, 2). These changes could be up to four times or more when glucose is distributed evenly around the rat body. At the same time, the level of the metabolized  $^{17}\text{O}$ -water was steadily increasing almost linear with the rate of ( $0.14 \pm 0.02 \text{ %/min}$ ) relative to the natural concentration of  $^{17}\text{O}$  water (20.7 mM). This rate of metabolized water increase is representing the rate of glucose consumption  $\text{CMR}_{\text{glc}} = 0.43 \pm 0.06 \text{ mmol/g tissue/min}$ . The observed steady rate of  $\text{CMR}_{\text{glc}}$  during the alteration of the glucose dose and the concentration in each experiment correlate with the observations of others specifying that glucose-6-phosphate (G-6-P) does not accumulate in hyperglycemia 1. The hexokinase that drives glucose phosphorylation only in one direction can serve as a gate. It can

be inhibited by the excess amount of G-6-P, which eventually can limit glucose consumption. Additional note: a complex calculation of the  $CMR_{glc}$  performed for mice 2 of  $0.07 \mu\text{mol/g}$  tissue/min looks incorrect. Our calculations by using a simple model 3 and the data from the mice experiments 2 gives  $CMR_{glc} = 0.62 \mu\text{mol/g}$  tissue/min.

**CONCLUSION** The rate of glucose metabolism in normal rats is consistent during dose variations of the injected glucose and alterations of glucose concentration after bolus injection. The phosphorylation of glucose by hexokinase could be a limiting factor for glucose availability during hyperglycemia or during application of the excessive amount of glucose.

**ACKNOWLEDGEMENTS** The study was performed at the National High Magnetic Field Laboratory (Tallahassee) supported by NSF, grant No. DMR-115490. Many thanks to Richard Desilets, Ashley Blue, Jason Kitchen, Steven Ranner, Peter Gor'kov and William Brey for their valuable help with RF probes.

## REFERENCES

1. Siesjo BK, Brain Energy Metabolism, 1978, John Wiley & Sons, Ltd.
2. Borowiak R, Reichardt W, Kurzhunov D, et al. Initial investigation of glucose metabolism in mouse brain using enriched  $^{17}\text{O}$ -glucose and dynamic  $^{17}\text{O}$ -MRS. NMR in Biomedicine, 2017; 30(8): e3724.
3. Fiat D, Kang S. Determination of the rate of cerebral oxygen consumption and regional cerebral blood flow by non-invasive  $^{17}\text{O}$  in vivo NMR spectroscopy and magnetic resonance imaging. Neurological Research, 1993; 15(7): 7-22.

## FIGURES

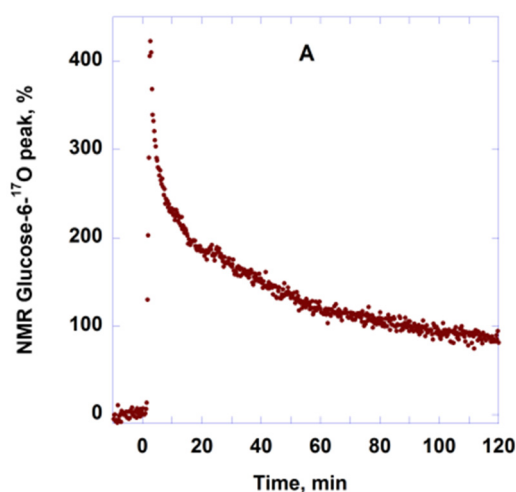


Fig. 1. Time course of  $^{17}\text{O}$  NMR peak of glucose-6- $^{17}\text{O}$  in rat head after 1.5 ml tale IV injection of glucose-6- $^{17}\text{O}$ /PBS solution. The oxygen enrichment was 47%, the total glucose dose was  $12 \mu\text{mol/g}$ . The corresponding changes of  $^{17}\text{O}$  water peak are presented at Fig. 2.

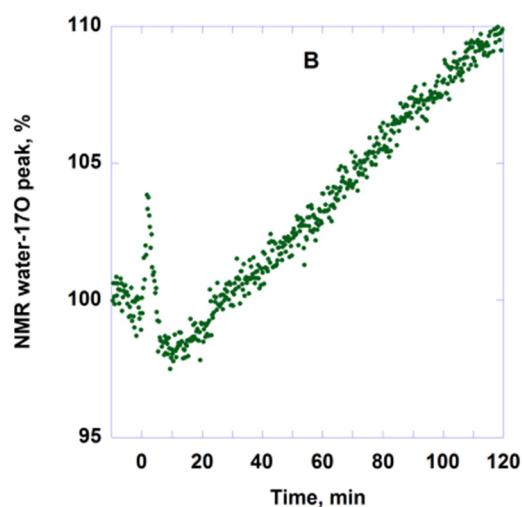


Fig. 2. Time course of  $^{17}\text{O}$  NMR water peak in rat head after the tail IV injection of glucose-6- $^{17}\text{O}$  during changes of glucose concentration, which are presented on Fig. 1. The oxygen enrichment was 47%; the total glucose dose was  $12 \mu\text{mol/g}$ .

## Using $^{129}\text{Xe}$ MR Imaging and Spectroscopic Signatures to Differentiate Pulmonary Arterial Hypertension from Other Cardiopulmonary Diseases

Elianna. A. Bier<sup>1,2</sup>, Ziyi Wang<sup>1,2</sup>, Aparna Swaminathan<sup>3</sup>, John Nouns<sup>2</sup>, Mu He<sup>2,4</sup>, Joseph G. Mammarrapallil<sup>5</sup>, Sheng Luo<sup>6</sup>, Sudarshan Rajagopal<sup>7</sup>, Bastiaan Driehuys<sup>1,2,5</sup>

<sup>1</sup>Department of Biomedical Engineering, Duke University, Durham, NC, USA

<sup>2</sup>Center for In Vivo Microscopy, Duke University Medical Center, Durham, NC, USA

<sup>3</sup>Division of Pulmonary, Allergy, and Critical Care, Department of Medicine, Duke University Medical Center, Durham, NC, USA

<sup>4</sup>Department of Electrical and Computer Engineering, Duke University, Durham, NC, USA

<sup>5</sup>Department of Radiology, Duke University Medical Center, Durham, NC, USA

<sup>6</sup>Department of Biostatistics & Bioinformatics, Duke University Medical Center, Durham, NC, USA

<sup>7</sup>Division of Cardiology, Department of Medicine, Duke University Medical Center, Durham, NC, USA

**SYNOPSIS:** This work sought to identify a non-invasive means to detect pulmonary arterial hypertension (PAH).  $^{129}\text{Xe}$  MRI and dynamic spectroscopy were acquired in healthy volunteers and subjects with chronic obstructive pulmonary disease (COPD), idiopathic pulmonary fibrosis (IPF), left heart failure (LHF), and PAH. COPD was differentiated from PAH by increased ventilation and barrier defects, while IPF was differentiated by increased barrier uptake. PAH and LHF subjects had similar imaging features but could be differentiated by their RBC signal oscillation amplitudes.  $^{129}\text{Xe}$  MR imaging and spectroscopy appears capable of differentiating PAH from COPD, IPF, and LHF.

**PURPOSE:** Unexplained dyspnea poses a significant problem for both patients and healthcare systems and is frequently worked up using invasive procedures. For example, a surgical lung biopsy may be performed to evaluate for interstitial lung disease or a right heart catheterization to evaluate for pulmonary arterial hypertension (PAH). Moreover, as more patients present with multiple co-morbidities it becomes increasingly difficult to determine whether PAH is contributing to their dyspnea and, thus, their optimal course of treatment. This problem may be addressed by combining  $^{129}\text{Xe}$  MR imaging to quantify regional gas exchange impairment with  $^{129}\text{Xe}$  spectroscopy to characterize cardiopulmonary dynamics. This work therefore sought to determine whether a non-invasive  $^{129}\text{Xe}$  MR study could identify signatures of regional gas exchange impairment and altered hemodynamics that differentiate PAH from other frequent causes of dyspnea, including chronic obstructive pulmonary disease (COPD), idiopathic pulmonary fibrosis (IPF), and left heart failure (LHF).

**METHODS:** The study included 22 healthy volunteers, 8 patients with COPD, 12 with IPF, 6 with LHF, and 10 with PAH.  $^{129}\text{Xe}$  imaging and spectroscopy were acquired on either a 1.5 GE 15M4 EXCITE or a 3T SIEMENS MAGNETOM Trio MRI scanner.

For each subject, 3D images were reconstructed from 1000 views each of an interleaved radial acquisition of gas- and dissolved-phase data during a breath hold. Acquisition used TR=15ms, flip angle of 0.5/20°, an echo time at which the two dissolved compartments were 90° out of phase ( $TE_{90}$ ) to permit decomposition, using the 1-point Dixon method, into RBC and barrier images.<sup>1</sup> The images were converted into binning maps depicting  $^{129}\text{Xe}$  ventilation, barrier tissue uptake, and red blood cell (RBC) uptake.<sup>2</sup> The three maps were quantified into percentages of the thoracic cavity exhibiting ventilation defect (VDP), barrier defect (BDP), high barrier (BHP), and RBC defect (RDP).<sup>3</sup>

Subjects underwent additional dynamic spectroscopy in which  $^{129}\text{Xe}$  free induction decays (FIDs) were collected every 20ms ( $TE=0.932\text{ms}$ , flip angle $\approx 20^\circ$ , dwell time=32 $\mu\text{s}$ , 512/1024 points). The FIDs from the breath-hold period were fit in the time domain to a model with 1 Voigt

(barrier) and 2 Lorentzian (RBC and gas) peaks. The time-dependent RBC signal amplitude and chemical shift were detrended and their cardiogenic oscillations were quantified by peak-to-peak amplitude.<sup>4</sup>

All statistics were performed using the Kruskal-Wallis test to test for differences between groups, and the Wilcoxon rank sum test for pairwise comparison.

**RESULTS:** Figure 1 shows ventilation and gas exchange maps for one representative subject from each cohort, and the quantitative imaging metrics for all subjects are compared in Figure 2. Compared to healthy volunteers, all disease cohorts exhibited increased VDP and RDP ( $p<0.001$  and  $p<0.001$ ). COPD patients exhibited significantly higher VDP and BDP compared to all other groups ( $VDP=39.0\pm24.5\%$ ,  $p<0.0001$ ;  $BDP=10.6\pm7.1\%$ ,  $p<0.0001$ ). IPF patients exhibited elevated barrier uptake compared to all other cohorts ( $BHP=39.8\pm29.3\%$ ,  $p<0.001$ ). PAH and LHF present with similar imaging characteristics to one another and exhibit mildly elevated VDP ( $PAH=6.2\%$ ,  $p=0.01$ ;  $LHF=10.4\%$ ,  $p=0.006$ ; vs healthy= $3.4\%$ ) and modestly elevated RDP ( $PAH=14.2\pm9.4\%$ ,  $p<0.001$ ;  $LHF=13.0\pm10.2\%$ ,  $p=0.01$ ; vs healthy= $2.6\pm1.5\%$ ).

Figure 3 shows the detrended RBC signal amplitude and chemical shift oscillations for these representative subjects, which are compared statistically in Figure 4. Compared to both healthy volunteers ( $9.4\pm2.7\%$ ,  $p=0.01$ ), and LHF ( $13.0\pm5.1\%$ ,  $p=0.007$ ), PAH presents with diminished RBC oscillations ( $6.0\pm3.6\%$ ). IPF is the only cohort to exhibit significant RBC chemical shift oscillations.

**DISCUSSION:** Imaging indicates that all diseases have a compound effect on both ventilation and RBC transfer relative to healthy subjects. Both COPD and IPF are distinguishable from the other cohorts by imaging metrics; COPD is characterized by elevated VDP and BDP, while IPF exhibits elevated BHP. However, PAH and LHF are indistinguishable on imaging, and it is only the dynamic spectroscopy that provides the additional cardiopulmonary dynamics that permit them to be differentiated. Specifically, PAH is caused by occlusions upstream of the pulmonary capillary bed, thus creating impedance to flow and diminishing the RBC signal oscillations. By contrast in post-capillary conditions such as LHF, high-impedance occurs downstream of the capillaries, and signal oscillations are enhanced. The RBC frequency oscillations uniquely seen in IPF are hypothesized to reflect delayed oxygenation.<sup>4</sup> Together, these metrics permit the application of a diagnostic algorithm such as illustrated in Figure 5 to determine the underlying causes of dyspnea.

**Conclusion:** <sup>129</sup>Xe MR imaging and spectroscopy are potentially powerful, non-invasive diagnostic tools for identifying pulmonary vascular disease in the setting of other pulmonary and cardiac co-morbidities. Future efforts will involve refining the diagnostic criteria proposed here and testing them in a blinded fashion against gold standard cardiac catheterization.

**ACKNOWLEDGEMENTS:** NIH/NHLBI R01 HL105643, NIH/NHLBI R01HL126771, and HHSN268201700001C

- (1) Kaushik SS, Robertson SH, Freeman MS, He M, Kelly KT, Roos JE, Rackley CR, Foster WM, McAdams HP, and Driehuys B. (2016), Single-breath clinical imaging of hyperpolarized <sup>129</sup>Xe in the airspaces, barrier, and red blood cells using an interleaved 3D radial 1-point Dixon acquisition. *Magn. Reson. Med.*, 75: 1434-1443. doi:10.1002/mrm.25675
- (2) Wang Z, Robertson, SH, Wang J, He M, Virgincar RS, Schrank GM, Bier EA, Rajagopal S, Huang YC, O'Riordan TG, Rackley CR, McAdams HP and Driehuys B. (2017), Quantitative analysis of hyperpolarized <sup>129</sup>Xe gas transfer MRI. *Med. Phys.*, 44: 2415-2428. doi:10.1002/mp.12264
- (3) Wang Z, He M, Bier EA, Rankine L, Schrank G, Rajagopal S, Huang YC, Kelsey C, Womack S, Mammarappallil J, Driehuys B. (2018). Hyperpolarized <sup>129</sup>Xe gas transfer MRI: The transition from 1.5T to 3T. *Magnetic Resonance in Medicine*. 10.1002/mrm.27377.
- (4) Bier EA, Robertson SH, Schrank G, Rackley C, Mammarappallil JG, Rajagopal S, McAdams HP, Driehuys B. A Robust Protocol for Quantifying Cardiogenic Oscillations in Dynamic <sup>129</sup>Xe Gas Exchange Spectroscopy: The Effects of Idiopathic Pulmonary Fibrosis NMR Biomed In Press 2018.

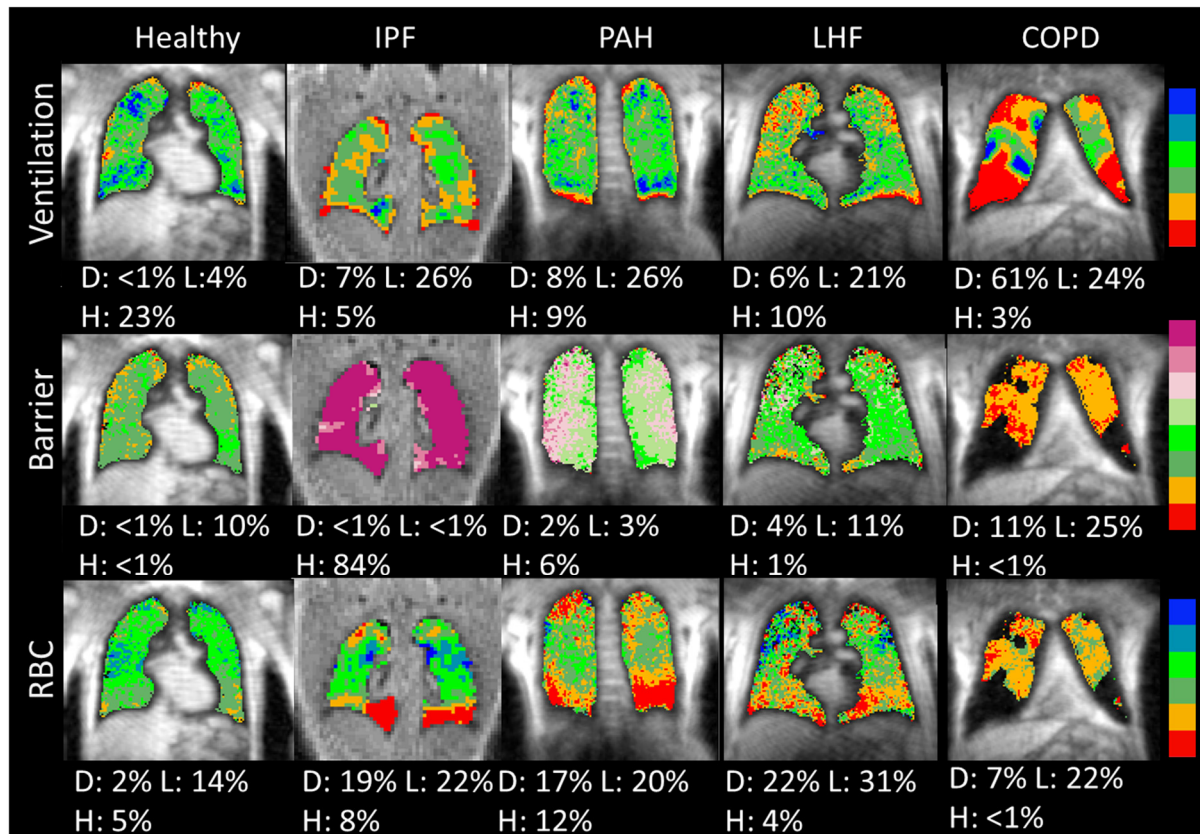


**Figure 1.** Ventilation, barrier:gas, and rbc:gas ratio maps for representative subjects from each cohort. Each map is quantified by the defect (D), low (L), and high (H), percentage. COPD uniquely exhibits very high VDP and regions of low barrier uptake (elevated BDP). IPF uniquely exhibits high barrier uptake. PAH and LHF both exhibit slightly elevated VDP and modestly elevated RDP.

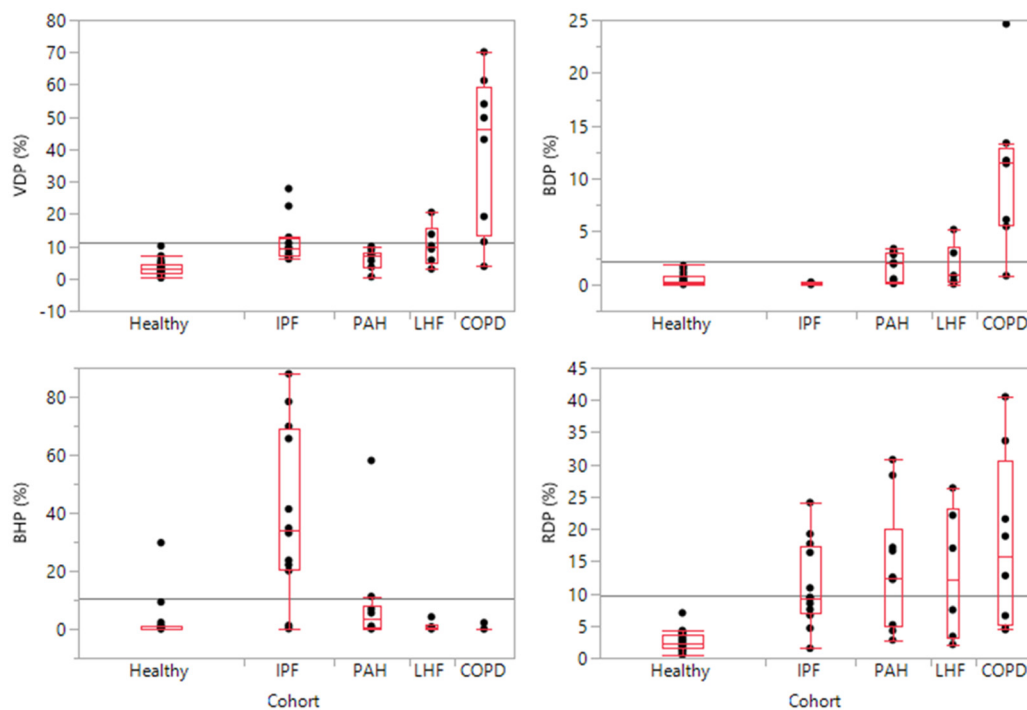


**Figure 2.** VDP, BDP, BHP, and RDP comparisons for all subjects. COPD is characterized by significantly elevated VDP and BDP. IPF uniquely exhibits high barrier uptake (elevated BHP). PAH and LHF both exhibit slightly elevated VDP and modestly elevated RDP, but these features alone do not permit them to be distinguished from the other cohorts.

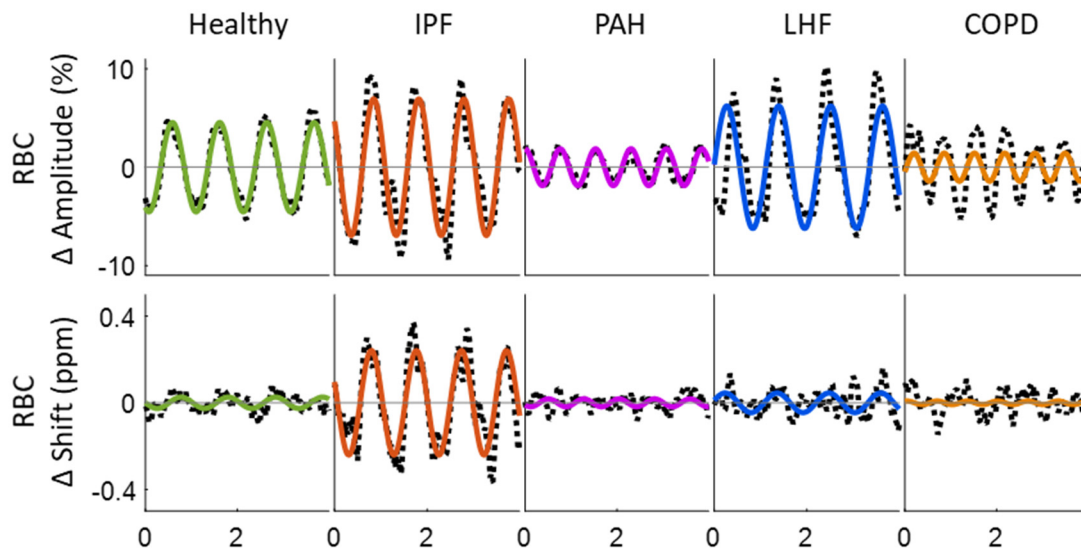


**Figure 3.** Detrended RBC signal amplitude and chemical shift oscillations that occur at the heart rate. IPF is the only cohort to exhibit oscillations in the RBC chemical shift. Both IPF and LHF exhibit enhanced RBC amplitude oscillations. By contrast, PAH exhibits diminished RBC signal oscillations compared to all other cohorts except COPD.

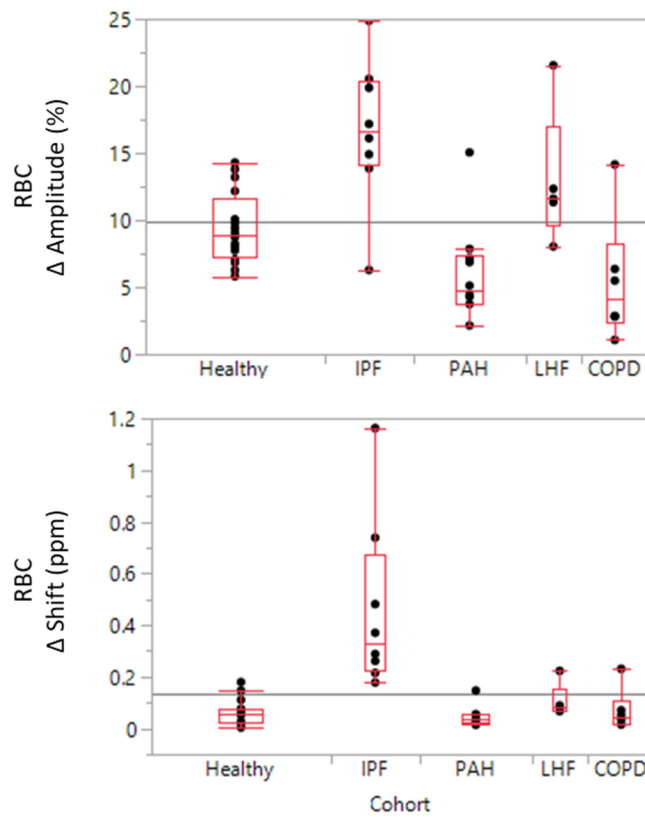


**Figure 4.** RBC signal amplitude and chemical shift oscillations for all subjects. PAH and LHF can be differentiated by the magnitude of the RBC amplitude oscillations. PAH is characterized by smaller oscillations, whereas LHF is characterized by larger RBC oscillations. Only IPF exhibits significant chemical shift oscillations.

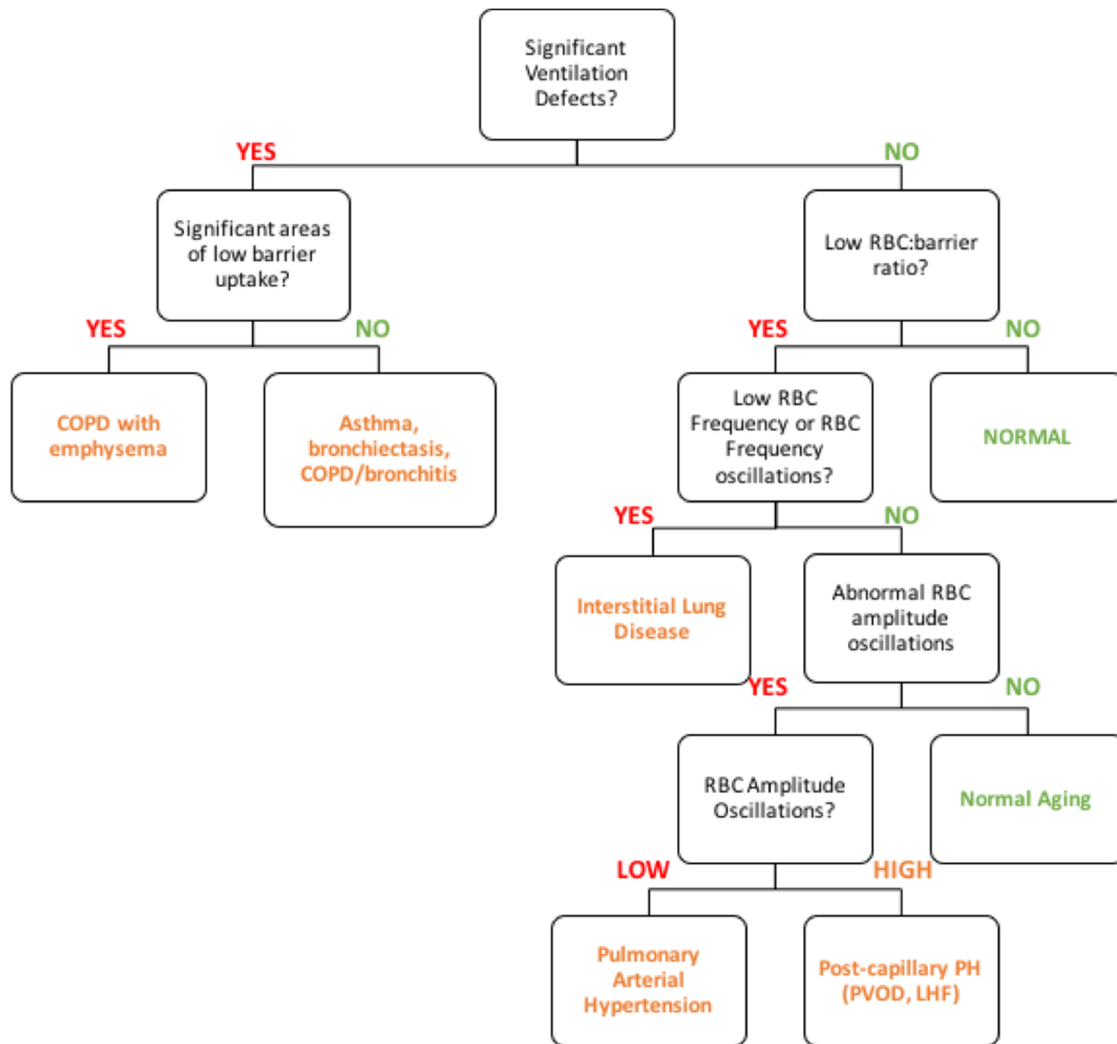


**Figure 5.** Possible diagnostic algorithm to differentiate obstructive, interstitial, and pulmonary vascular conditions based on  $^{129}\text{Xe}$  imaging and spectroscopic metrics.

## A Real-Time Centralized Pipeline for Reconstructing and Quantifying Hyperpolarized $^{129}\text{Xe}$ Gas Exchange MRI

Ziyi Wang<sup>1</sup>, Mu He<sup>2</sup>, Alex Culbert<sup>1</sup>, John Nouns<sup>3</sup>, Elianna Bier<sup>1</sup>, and Bastiaan Driehuys<sup>1, 2, 3</sup>

<sup>1</sup>Biomedical Engineering, Duke University, Durham, North Carolina, United States, <sup>2</sup>Department of Electrical and Computer Engineering, Duke University, Durham, NC, USA, <sup>3</sup>Radiology, Duke University Medical Center, Durham, North Carolina, United States

**SYNOPSIS:** Hyperpolarized  $^{129}\text{Xe}$  MRI is emerging as a powerful means to provide 3D quantitative mapping of ventilation, interstitial barrier uptake, and red blood cell transfer. However, this capability requires non-standard radial reconstruction and accurate lung segmentation to enable quantitative analysis. Such reconstruction and image processing would ideally be standardized and centralized to facilitate using  $^{129}\text{Xe}$  gas exchange MRI in multi-center clinical trials. To this end, we developed a neural-network based lung segmentation approach that automatically generates accurate masks. With this capability, we demonstrate a fully centralized processing pipeline for real-time reconstruction and quantitative reporting of  $^{129}\text{Xe}$  gas exchange MRI.

**INTRODUCTION:** Recently it has become possible for hyperpolarized  $^{129}\text{Xe}$  MRI to provide 3D quantitative mapping of ventilation, interstitial barrier uptake, and red blood cell (RBC) transfer from two inhalations of xenon [1]. However, this capability requires non-standard radial acquisition and reconstruction as well as accurate thoracic cavity segmentation to enable quantitative analysis. To facilitate and accelerate adoption of this capability for multi-center clinical trials, it is desirable to centralize and standardize the reconstruction and image

processing procedure. Arguably, the most significant obstacle for such quantitative mapping lies in obtaining an accurate thoracic cavity segmentation. To overcome this hurdle in automatic processing, we have developed an automatic segmentation method based on neural networks, utilizing multi-channel information from both proton and  $^{129}\text{Xe}$  images. With this capability, we demonstrate a centralized pipeline for real-time image reconstruction and quantitative reporting of  $^{129}\text{Xe}$  gas exchange images.

**METHODS:** The study enrolled 80 subjects who underwent an imaging protocol consisting of a calibration spectroscopy, a breath-hold 3D radial  $^{129}\text{Xe}$  ventilation/dissolved-phase image, and a breath-hold  $^1\text{H}$  UTE image, as detailed in [2]. All imaging was conducted on a 3T scanner (Siemens MAGNETOM Trio). The pipeline is designed to facilitate the study without human intervention (Figure 1). It consists of 3 major units to facilitate calibration and parameter setting, image reconstruction and quantification, and clinical reporting (Figure 2). The pipeline was implemented on a workstation running the Ubuntu operating system and operates as follows. First, the  $^{129}\text{Xe}$  calibration raw file acquired on the scanner is saved to a shared-access folder, where it is detected by the pipeline's scout program, which launches its Calibration unit. This calculates parameters for setting scanner frequency, transmit voltages, and the TE required for Dixon-based separation of RBC and barrier images. These results are sent to the MR technologist using the Twilio (<https://www.twilio.com>) SMS text service, thereby allowing the subsequent imaging sequence to be prescribed. Once the  $^{129}\text{Xe}$  gas exchange and anatomical  $^1\text{H}$  raw data have been acquired and saved to the shared folder, the Image Quantification unit is launched and completes image reconstruction (using compiled C code for speed). After reconstruction, it segments the thoracic cavity (using a neural network model described below) and registers the resulting mask to the functional  $^{129}\text{Xe}$  MRI scan (using Simple-ITK). The  $^{129}\text{Xe}$  ventilation data is bias-field corrected (N4BiasfieldCorrection[3]), and then thresholded to produce color binning maps of ventilation[4]. Similar processing is applied to barrier uptake and RBC transfer, but since these are expressed as a ratio relative to the gas-phase image, the source images are not bias-field corrected [5]. The maps and the related quantitative metrics are then passed to the Report Generation unit to render clinical report using a HTML template. The report is immediately delivered via an email in PDF and PPT format, making it accessible from mobile devices. The unit also archives NIFTI files of the color maps and populates a running CSV file with the subject ID and the derived quantitative image metrics.

The neural network model for segmentation (Figure 3) employs both the  $^1\text{H}$  and  $^{129}\text{Xe}$  images. It consists of a down-sampling encoder (to extract image features), feature fusion layers (to incorporate the features), and an up-sampling decoder (to restore image resolution), with down-sampling indices preserved to retain high-frequency information [6]. The model was trained using 3D  $^1\text{H}$  anatomical and  $^{129}\text{Xe}$  ventilation images from 116 scans, that were manually segmented in ITK-Snap (<http://www.itksnap.org>). Training involved minimizing the Mean Squared Error (MSE) loss between the model output and the manually segmented masks.

**RESULTS:** The calibration result (text message) is delivered around 30 seconds after the calibration scan has been saved. The final clinical report (email) is delivered within 3 minutes of scan completion. Figure 4 shows representative segmentations of the thoracic  $^1\text{H}$  images using the neural network model. Its accuracy was found to be improved by incorporating  $^{129}\text{Xe}$  ventilation image data to clarify regions of unclear boundaries such as the ribs and stomach. Such ventilation imaging was found to be useful even when ventilation defects are present. A representative quantitative report is shown in Figure 5, depicting a COPD patient with ventilation defects, diminished barrier uptake (emphysema) and poor RBC transfer.

**DISCUSSION:** The pipeline described now provides routine, real-time data processing and clinical report generation without human intervention. Moreover, its centralized implementation and rapid delivery positions the system well to ultimately provide remote service through secure, HIPAA-compliant online data transfer. This capability could provide a useful means to standardize image reconstruction and processing procedures to facilitate multi-center studies incorporating gas exchange MRI.

**Acknowledgements:** IH/NHLBI R01 HL105643, NIH/NHLBI R01HL126771, and HHSN268201700001C

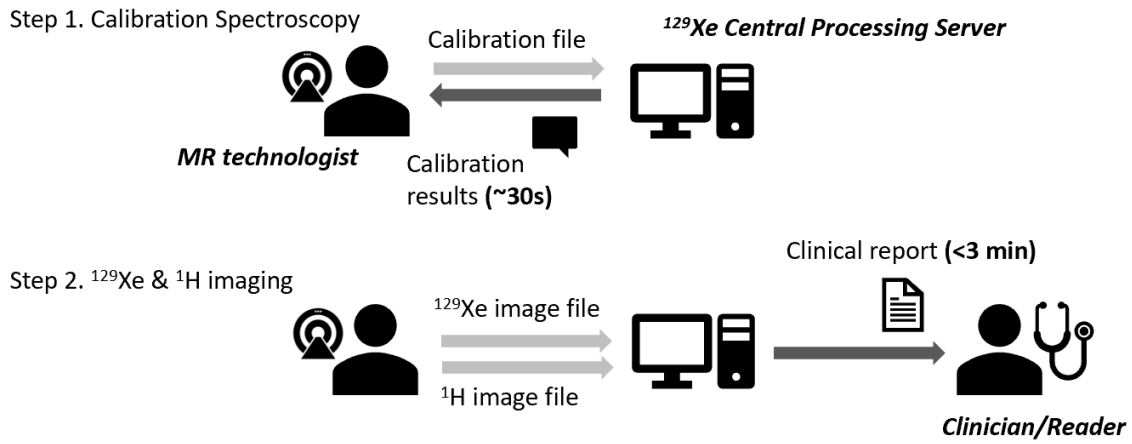


**Figure 1.** The  $^{129}\text{Xe}$  central processing server facilitates the acquisition and processing of  $^{129}\text{Xe}$  gas exchange MRI. The server reports calibration results within 30 seconds of scan completion/file save and delivers the final clinical report within 3 minutes of completion/saving of the imaging scans. Beyond the technologist operating the scanner and saving data, no additional intervention is required.

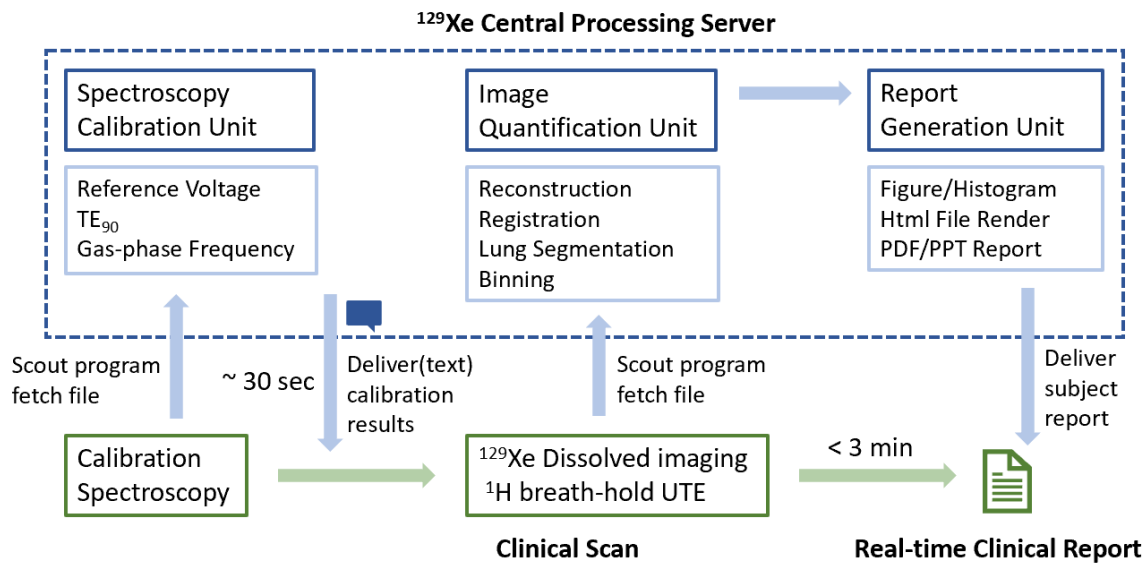


**Figure 2.** The pipeline consists of 3 units: Spectroscopy Calibration, Image Quantification, and Report Generation. The Spectroscopy Calibration unit calculates scanner reference voltage, echo time when RBC and barrier are 90-degree out-of-phase ( $\text{TE}_{90}$ ), and  $^{129}\text{Xe}$  gas-phase resonance frequency. These are immediately reported (with SMS text) and used to prescribe the subsequent imaging sequences. The Image Quantification unit fetches files from both the anatomical  $^1\text{H}$  and functional  $^{129}\text{Xe}$  scans, reconstructs and parses the images, and conducts the quantification. The Report Generation unit then produces a clinical report through HTML rendering with the images. The report is delivered within 3 minutes after completion of both scans.

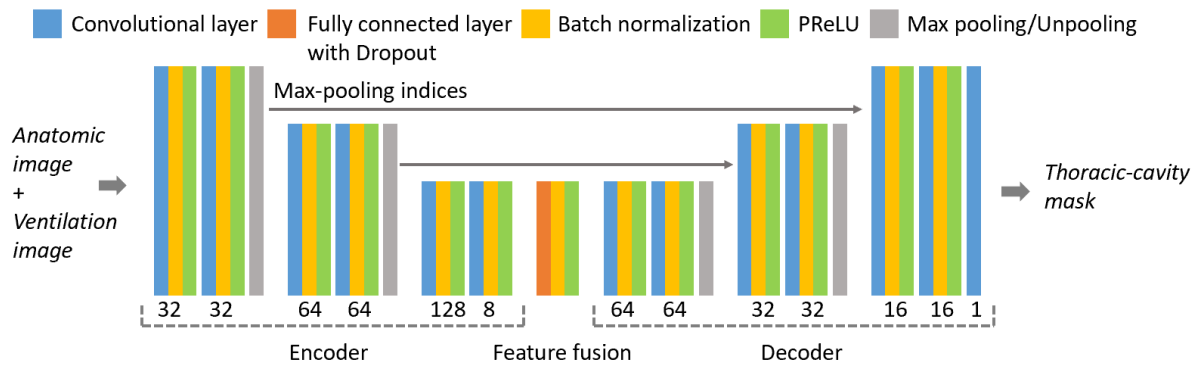


**Figure 3.** Neural network model inputs anatomic  $^1\text{H}$  and functional  $^{129}\text{Xe}$  images to obtain a binary thoracic cavity segmentation. The model consists of a down-sampling encoder, feature fusion layers, and an up-sampling decoder. The encoder is composed of convolutional layers (3×3 filter size, number of filters noted on the figure), batch-normalization, PReLU activation [7], and max-pooling layers. The feature-fusion layers use a fully-connected layer (with 25% Dropout) to merge the 8-channel features. The decoder has a structure that is symmetric to that of the encoder to restore the image resolution. The max-pooling indices are saved for unpooling to retain the high frequency information.

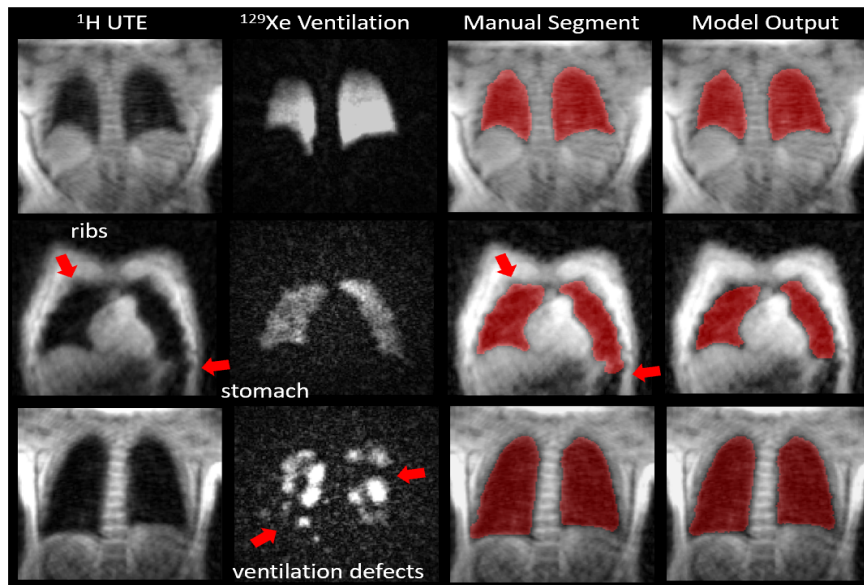


**Figure 4.** Representative thoracic cavity masks for 3 subjects generated by manual segmentation versus with the convolutional neural network (CNN) model. The model was trained with manual segmentation generated using the active-contour method in ITK-Snap. The CNN model produces accurate lung segmentations, employing both  $^1\text{H}$  UTE and  $^{129}\text{Xe}$  ventilation images. The  $^{129}\text{Xe}$  ventilation image provides additional information that resolves unclear lung boundaries caused by the ribs and stomach (second row). Inclusion of  $^{129}\text{Xe}$  ventilation still produces high quality lung segmentation, even when substantial ventilation defects are present (third row).

### Gas Exchange Summary of Subject 001

scan: 18-08-29; processed: 18-10-19

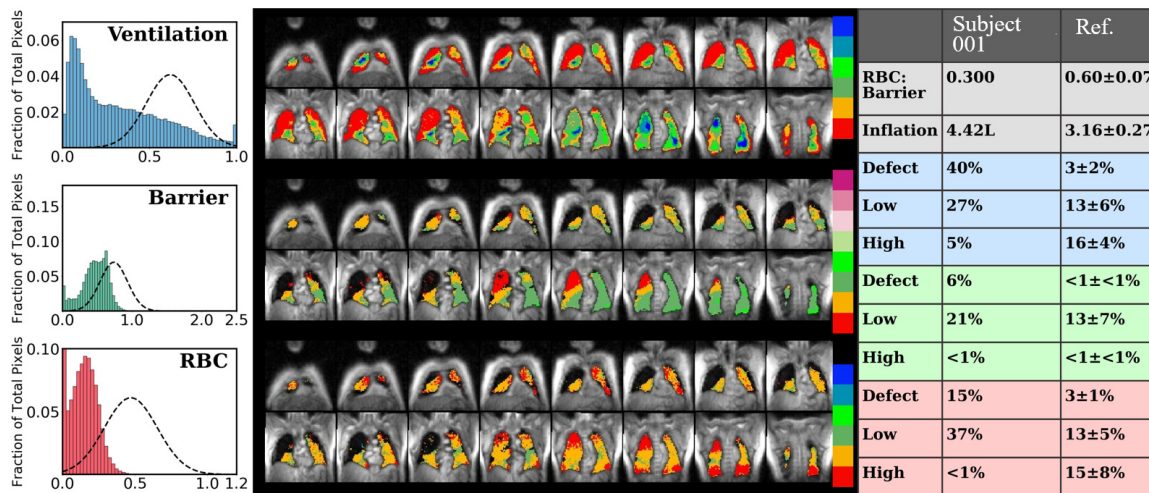


**Figure 5.** Representative quantitative clinical report in a COPD patient (FEV1: 66%, FEV1/FVC: 68%, FEF25-75: 22%, DLCO: 39%). The left panel shows the distributions of ventilation, barrier uptake and RBC transfer in the lungs of the patient relative to the dashed lines that reflect the healthy reference distributions. The middle panel contains multi-slice montages of each of the 3 maps. The right panel shows the quantitative metrics derived from each map for the patient and shows how they compare to healthy reference values. This patient shows substantial ventilation defects, barrier uptake defects and diminished RBC transfer.

### References:

1. Kaushik, S.S., et al., Single-breath clinical imaging of hyperpolarized ( $^{129}\text{Xe}$ ) in the airspaces, barrier, and red blood cells using an interleaved 3D radial 1-point Dixon acquisition. *Magn Reson Med*, 2016. 75(4): p. 1434-43.
2. Wang, Z., et al., Hyperpolarized ( $^{129}\text{Xe}$ ) gas transfer MRI: the transition from 1.5T to 3T. *Magn Reson Med*, 2018.
3. Tustison, N.J., et al., N4ITK: Improved N3 Bias Correction. *Ieee Transactions on Medical Imaging*, 2010. 29(6): p. 1310-1320.
4. He, M., et al., Extending semiautomatic ventilation defect analysis for hyperpolarized ( $^{129}\text{Xe}$ ) ventilation MRI. *Acad Radiol*, 2014. 21(12): p. 1530-41.
5. Wang, Z., et al., Quantitative analysis of hyperpolarized  $^{129}\text{Xe}$  gas transfer MRI. *Med Phys*, 2017. 44(6): p. 2415-2428.
6. Badrinarayanan, V., A. Kendall, and R. Cipolla, SegNet: A Deep Convolutional Encoder-Decoder Architecture for Image Segmentation. *Ieee Transactions on Pattern Analysis and Machine Intelligence*, 2017. 39(12): p. 2481-2495.
7. He, K.M., et al., Delving Deep into Rectifiers: Surpassing Human-Level Performance on ImageNet Classification. 2015 *Ieee International Conference on Computer Vision (Iccv)*, 2015: p. 1026-1034.

# Our ISMRM booth wall 2019

*Your global supplier for stable isotopes*



**$^{17}\text{O}$  in the form of water, gas and D-Glucose**

**$^{17}\text{Oxygen}$**   
is the only non-radioactive isotope to measure oxygen consumption and metabolism in real-time by using MRI systems for diagnostic applications and medical research.

**$^{18}\text{Oxygen}$**   
is used to synthesize radiopharmaceuticals labelled with Fluorine-18 (for example 2-fluoro-2-deoxy glucose [ $^{18}\text{F}$ FDG]). These are used for Positron Emission Tomography (PET), the most common cancer diagnostic technique.

**$^{15}\text{Nitrogen}$**   
is used to produce  $^{15}\text{N}$  labelled chemical compounds for medical and biomedical applications as well as improving the harvest in agriculture.

**$^{129}\text{Xe}$  in the form of pure gas and mixtures**

**$^{129}\text{Xenon}$**   
in the hyperpolarized state is a revolutionary novel MRI contrast agent for diagnostic purposes.  $^{129}\text{Xe}$  facilitates the taking of high-resolution 3D lung images by using a conventional MRI scanner.

**$^{10}\text{B}$  in the form of salts and gas**

**$^{10}\text{B}$  in the form of water**

With courtesy of Proton Imaging Ltd.

With courtesy of Duke University, Durham, NC.

**Realizing ideas with isotopes**

[nukem-isotopes.com](http://nukem-isotopes.com)

## Information about our booth wall

The  $^1\text{H}/^{17}\text{O}$ -MRI images and diagrams on our wall (top, left side) were, thankfully, provided by the German Cancer Research Center (DKFZ), Heidelberg, Germany and University Hospital Erlangen, Erlangen, Germany.

The displayed images and diagrams are part of an ongoing study and are presented at the ISMRM in the abstract entitled “Metabolic Rate of Oxygen Consumption in Brain Tumors: A pilot  $^{17}\text{O}$  MRI study”.

In addition, the MRI lung images (on the right side) were, thankfully, provided by Duke University, Durham, NC (Bastiaan Driehuys) and the image of the Xe-129 Polarizer was gratefully provided to us by our business partner Polarean.

# Oxygen-17 bibliography

## ISMRM 2018 abstract/presentations

1. Sebastian C. Niesporek, Reiner Umathum, Jonathan M. Lommen, and Armin M. Nagel; Direct Partial Volume Corrected CMRO<sub>2</sub> Determination: Simulation assisted Dynamic <sup>17</sup>O-MRI; Abstract #2955
2. Dmitry Kurzhunov, Jan Sedlacik, Robert Borowiak, Divya Sanam Bolar, Johannes Fischer, Ali Caglar Özen and Michael Bock, Quantification of Oxygen Metabolism in Human Brain: Comparison of Direct <sup>17</sup>O with Indirect <sup>1</sup>H MR Method. Abstract #3689
3. Victor D. Schepkin, Andreas Neubauer, Christian Schuch, Tilo Glaeser, Michael Kievel, Steven L. Ranner, William W. Brey, Shannon Helsper, and Lothar Schad; The first observation of <sup>17</sup>O MRI in normal rats at 21.1 T; Abstract #4546

## ISMRM 2017 abstracts/presentations

4. Sebastian C. Niesporek, Reiner Umathum, Jonathan M. Lommen, and Armin M. Nagel; Direct Partial Volume Corrected CMRO<sub>2</sub> Determination: Simulation assisted Dynamic <sup>17</sup>O-MRI; Abstract #2955
5. Victor D. Schepkin, Andreas Neubauer, Christian Schuch, Tilo Glaeser, Michael Kievel, Steven L. Ranner, William W. Brey, Shannon Helsper, and Lothar Schad; The first observation of <sup>17</sup>O MRI in normal rats at 21.1 T; Abstract #4546
6. Hannes Michel Wiesner, Dávid Zsolt Balla, Klaus Scheffler, Kamil Ugurbil, Xiao-Hong Zhu, Wei Chen, Kamil Uludag, and Rolf Pohmann; Simultaneous measurement of metabolic rates of oxygen via <sup>17</sup>O NMR imaging in brain and muscle tissue of rat at 16.4T; Abstract #5623
7. Dmitry Kurzhunov, Robert Borowiak, Marco Reisert, Axel Joachim Krafft, and Michael Bock; Direct ESTimation of <sup>17</sup>O MR ImageS (DIESIS) for CMRO<sub>2</sub> Quantification in the Human Brain with Partial Volume Correction; Abstract #0488
8. Dmitry Kurzhunov, Robert Borowiak, Marco Reisert, Axel Joachim Krafft, Ali Caglar Özen and Michael Bock; 3D CMRO<sub>2</sub> Mapping in Human Brain with Direct <sup>17</sup>O-MRI: Comparison of Methods for Image Reconstruction and Partial Volume Correction; Abstract #3602
9. Dmitry Kurzhunov, Robert Borowiak, Ali Caglar Özen, and Michael Bock; CMRO<sub>2</sub> Quantification in Human Brain with Direct <sup>17</sup>O-MRI: Profile Likelihood Analysis for Optimization of Temporal Resolution; Abstract #0568
10. Robert Borowiak, Wilfried Reichardt, Dmitry Kurzhunov, Christian Schuch, Benjamin Görling, Dieter Leibfritz, Jochen Leupold, Thomas Lange, Helge Haas, Jens Timmer, and Michael Bock; Quantification of Cerebral Metabolic Rates of <sup>17</sup>O-Labeled Glucose in Mouse Brain with Dynamic <sup>17</sup>O-MRS; Abstract #2954
11. Hannes Michel Wiesner, Yi Zhang, Ming Lu, Nanyin Zhang, Xiao-Hong Zhu, and Wei Chen; Measurement of CMRO<sub>2</sub> in conscious rat with in vivo <sup>17</sup>O MRS at 16.4T; Abstract #2953

## ISMRM 2016 abstracts/presentations

1. Dmitry Kurzhunov, Robert Borowiak, Marco Reisert, Philipp Wagner, Axel Krafft, and Michael Bock; 3D CMRO<sub>2</sub> mapping in human brain with direct <sup>17</sup>O-MRI and proton-constrained iterative reconstructions; Program Number 1470
2. Hannes Michel Wiesner, Xiao-Hong Zhu, Kamil Ugurbil, and Wei Chen; Sensitivity Comparison of Ultrahigh-field Oxygen-17 MRS Imaging between 7T and 10.5T using a Human Head Size Phantom and Quadrature Surface Coil; Program Number: 3942
3. Ruomin Hu, Andreas Neubauer, Jorge Chacón-Caldera, Javier Uranga Solchaga, Christian Schuch, Tilo Gläser, Cordula Nies, Eric Gottwald, Stefan Giselsbrecht, and Lothar R. Schad; In Vitro Oxygen-17 NMR Spectroscopy of Cellular Metabolism at Ultra High Field; Program Number 3963
4. Robert Borowiak, Wilfried Reichardt, Dmitry Kurzhunov, Christian Schuch, Jochen Leupold, Thomas Lange, Marco Reisert, Axel Krafft, Elmar Fischer, and Michael Bock; Initial investigation of glucose metabolism in mouse brain using enriched <sup>17</sup>O-glucose and dynamic <sup>17</sup>O-MRS; Program Number 3964

5. Sebastian C. Niesporek, Reiner Umathum, Thomas M. Fiedler, and Armin M. Nagel; Evaluation of High Temporal and Spatial Resolution  $^{17}\text{O}$ -MRI; Program Number 3965
6. Sebastian C. Niesporek, Reiner Umathum, Thomas M. Fiedler, and Armin M. Nagel; Iterative Approach for Partial Volume Corrected T2\* Determination in  $^{17}\text{O}$ -MRI; Program Number 3966

#### **ISMRM 2015 abstracts/presentations**

1. Borowiak, R., Kurzhunov, D., Wagner, P., Reiser, M., Bock; Dynamic  $^{17}\text{O}$ -MRI at 3 Tesla for In Vivo CMRO<sub>2</sub> Quantification; Program Number: 4633
2. Zhang, Y., Erokwu, B. O., Liu, Y., Farr, G. W., Boron, W. F., Flask, C. A., Yu, X.; Assessing Water Influx and Retention in the Brain of AQP4 Knockout Mice by  $^{17}\text{O}$ -MRI; Program Number: 1997.
3. Najac, C., Tiret, B., Flament, J., Guillermier, M., Houitte, D., Badin, R.A., Hantraye, P., Brouillet, E., Lebon, V., Valette, J., CMRO<sub>2</sub> Quantification by Direct  $^{17}\text{O}$  MRI at 7 T in the Macaque Brain: Assessment of Energy Metabolism Impairment In Vivo; Program Number: 4615.
4. Zhu, X-H., Wiesner, H. M., Lee, B-Y., Lu, M., Ugurbil, K., Chen, W.; Quantitative and Simultaneous Imaging of CMRO<sub>2</sub>, CBF and OEF in Resting Human Brain; Program Number: 0895.

#### **ISMRM 2014 abstracts/presentations**

1. Borowiak, R., Groebner, J., Kurzhunov, D., Fischer, E., Dragonu, I., Bock, M.; Direct Cerebral  $^{17}\text{O}$ -MRI at a Clinical Field Strength of 3 Tesla Using a Tx/Rx Head Coil; Program Number: 0687.
2. Zhu, X-H., Liu, X., Lu, M., Wiesner, H M., Ugurbil, K., Chen, W.; In Vivo  $^{17}\text{O}$  MR Imaging and Quantification of CMRO<sub>2</sub>, CBF and OEF in Human Visual Cortex at Rest and During Activation; Program Number: 3763.
3. Augath, M A., Seuwen, A., Zwick, S., Rudin, M.; Increase in Sensitivity and Signal Stability in  $^{17}\text{O}$  MRI Using a Cryogenic RF Probe; Program Number: 2972.
4. Möllenhoff, K., Felder, J., Romanzetti, S., Gordji-Nejad, A., Shah, N J., Natural Abundance in Vivo  $^{17}\text{O}$  Measurements at 9.4T; Program Number: 0475.
5. Barbier, E., Mapping Blood Flow & Tissue Oxygenation with MRI: Insights from Other Modalities
6. Cerdán, S.; Subject: Bamboc; MR Spectroscopy: The Promise; Program Number: 1027.

#### **ISMRM 2013 abstracts/presentations**

1. Romanzetti, S., Fiege, D. P., Shah, N.J., 3D TWIRL: A Novel K-Space Trajectory for Imaging of Fast Relaxing Nuclei; Program Number: 3965.
2. Hoffmann, S. H., Meise, F. M., Biller, A., Nagel, A. M.; Adaptive Combination of Multichannel Data for Non-Proton MRI; Program Number: 1983.
3. Groebner, J., Borowiak, R., Rösler, M., Umathum, R., Fischer, E., Pavlina, J. M., Bock, M.; In Vivo  $^{17}\text{O}$ -MRI at 3 Tesla Using a TxRx Surface Coil; Program Number: 1985.
4. Lee, J.-H., Norris, M., Fugate, E. M., Avdievich, G. I., Hetherington, H. P.; A Novel Double Tuned 4T  $^1\text{H}/^{17}\text{O}$  Head Volume Coil; Program Number: 2784.
5. Cui, W., Zhu, X.-H., Vollmers, M., Colonna, E., Adriany, G., Tramm, B., Dubinsky, J., Oz, G., Oxygen-17 MRS for CMRO<sub>2</sub> Measurements in the Mouse Brain at 16.4T; Program Number: 0863.
6. Hoffmann, S. H., Radbruch, A., Semmler, W., Nagel, A. M.; . Partial Volume Corrected CMRO<sub>2</sub> Determination in a Glioblastoma Patient by  $^{17}\text{O}$  MRI; Program Number: 0216.
7. Wang, X., Zhu, X.-H., Zhang, Y., Chen, W., Significant BOLD Signal Reduction Induced by Perfluorocarbon Emulsion in the Rat Brain; Program Number: 0848.
8. Boros, E., Polasek, M.v., Zhang, Z., Caravan, P.A.; Single Amino Acid Gd-Complex as a Modular Tool for High Relaxivity MR Contrast Agent Development; Program Number: 1900.
9. Atkinson, I. C., Ultra-High Field MR: Multi-Nuclear Imaging, Symposium - Emerging Technologies for Clinical Neuroimaging; Program Number: 007006

#### **ISMRM 2012 abstracts/presentations**

1. Pilkinton, D. T., Babu, V. K., Baker, W., Greenberg, J. H., Reddy, R., Hyperoxic Calibrated Quantitative fMRI for the Measurement of Regional Cerebral Metabolic Rate of Oxygen in a Hypermetabolic Swine Model; *Program; Proc. Intl. Soc. Mag. Reson. Med.* 20 (2012); Number: 2912

2. Zhu, X.-H., Chen, W., In Vivo  $^{17}\text{O}$  Measurements of Water Rotational Correlation Time and Hydrodynamic Radius in Rat Brain; *Proc. Intl. Soc. Mag. Reson. Med.* 20 (2012); Program Number: 1821
3. Wiener, E. C., Sengar, R., Elst, L. V., Abadjian, M.-C., Moore, C.E., Rheingold, A. L., Grotjahn, D., New Bifunctional Chelates with Optimal Water Residence Times for Molecular Imaging; *Proc. Intl. Soc. Mag. Reson. Med.* 20 (2012); Program Number: 0793
4. Zheng, J., Muccigrosso, D., Bashir, A., Gupte, P., Gropler, R. J.; Quantitative Cardiac  $^{17}\text{O}$  MRI: Initial Validation Study; *Proc. Intl. Soc. Mag. Reson. Med.* 20 (2012); Program Number: 3887.
5. Liu, P., Xu, F., Lu, H.; A Turn-Key Solution for the Quantification of Brain Oxygen Metabolism; *Proc. Intl. Soc. Mag. Reson. Med.* 20 (2012); Program Number: 471.

#### **ISMRM 2011 abstracts/presentations**

1. Atthe B, Kemerer M, Chen Y, et al. Quantitative Assessment of Mitochondrial Metabolic Efficiency by  $^{17}\text{O}$  and  $^{31}\text{P}$  MR Spectroscopy in Isolated Rat Hearts. *Proc. Intl. Soc. Mag. Reson. Med.* 19 (2011).
2. Muccigrosso D, He X, Abendschein D, et al. Methods for Quantification of Absolute Myocardial Oxygen Consumption with  $^{17}\text{O}$ -CMR. *Proc. Intl. Soc. Mag. Reson. Med.* 19 (2011).
3. Meise FM, Groebner J, Nagel AM, et al. A 30-Channel Phased Array for Oxygen-17 ( $^{17}\text{O}$ ) Brain MRI at 7 Tesla. *Proc. Intl. Soc. Mag. Reson. Med.* 19 (2011).
4. Hoffmann SH, Nagel AM, Meise FM, Umathum R, Bock M. In Vivo Relaxation Parameters of Oxygen-17 ( $^{17}\text{O}$ ). *Proc. Intl. Soc. Mag. Reson. Med.* 19 (2011).
5. Zhu X-H, Chen J, Tu T-W, Chen W, Song S-K. Exploring the New Utility of the  $^{17}\text{O}$ -MRS Imaging Technique for Studying CMRO<sub>2</sub> and Perfusion in Stroke Mice. *Proc. Intl. Soc. Mag. Reson. Med.* 19 (2011).
6. Wiesner HM, Pohmann R, Balla DZ, Chen W, Ugurbil K, Uludag K. Measurement of CMRO<sub>2</sub> Changes by Somatosensory Stimulation in Rat Using Oxygen-17 at 16.4T. *Proc. Intl. Soc. Mag. Reson. Med.* 19 (2011).
7. Kassey VB, Baker W, Mesquita RC, et al. Preliminary Studies to Assess CMRO<sub>2</sub> with Integrated T1 Rho MRI and Hybrid DRS/DCS Optical Approach in Clinical Scanners. *Proc. Intl. Soc. Mag. Reson. Med.* 19 (2011).
8. Mateescu GD, Flask CA, Duerk JL. Novel Approach for the Assessment of the Bioavailability of Exogenous Phosphate by in Vivo Dynamic  $^{17}\text{O}$  and  $^{31}\text{P}$  MRS and MRI. *Proc. Intl. Soc. Mag. Reson. Med.* 19 (2011).
9. Lu M, Wang X, Taylor R, et al. In Vitro and In Vivo Studies of  $^{17}\text{O}$  NMR Sensitivity at 9.4 and 16.4 Tesla. *Proc. Intl. Soc. Mag. Reson. Med.* 19 (2011).
10. Kirsch S, Schad LR. Single-Slice Mapping of Submillisecond T2 Using Spin Echo Prepared Ultra-Short Echo Time Imaging. *Proc. Intl. Soc. Mag. Reson. Med.* 19 (2011).

#### **ISMRM 2010 abstracts/presentations**

1. Zhu X-H, Zhang Y, Chen W. In Vivo  $^{17}\text{O}$  MRS Imaging for Assessing Myocardial Oxygen Metabolism in Rat Heart at 9.4T. *Proc. Intl. Soc. Mag. Reson. Med.* 18 (2010).
2. Zhu X-H, Zhang Y, Wiesner H, Ugurbil K, Chen W. Estimation of CBF Based on the Metabolic  $\text{H}_2^{17}\text{O}$  Decay Rate in CMRO<sub>2</sub> Measurement Using In Vivo  $^{17}\text{O}$  MR Approach. *Proc. Intl. Soc. Mag. Reson. Med.* 18 (2010).
3. Hoffman S, Begovatz P, Nagel A, Umathum R, Bock M. In Vivo Oxygen-17 ( $^{17}\text{O}$ ) MRI at 7 Tesla. *Proc. Intl. Soc. Mag. Reson. Med.* 18 (2010).
4. Wey H-Y, Du F, Lin A-L, et al. Indirect  $^{17}\text{O}$  MRI Using T1ρ at 11.7 T. *Proc. Intl. Soc. Mag. Reson. Med.* 18 (2010).
5. Narazaki M, Kanazawa Y, Ikehira H, Matsuda T. The  $^{17}\text{O}$  Imaging for Regional Oxygen Consumption Rate in Tumor Bearing Mice at 7T. *Proc. Intl. Soc. Mag. Reson. Med.* 18 (2010).
6. Lu M, Spires J, Mateescu GD, Flask C, Yu X. Exploration of Mitochondrial Respiration in Isolated Hearts: An Observation from Metabolically Produced  $\text{H}_2^{17}\text{O}$  Using  $^{17}\text{O}$  NMR Spectroscopy. *Proc. Intl. Soc. Mag. Reson. Med.* 18 (2010).
7. Atkinson IC, Sonstegaard R, Bitou L, Pliskin NH, Thulborn KR. Safety of  $^{17}\text{O}$  and  $^{23}\text{Na}$  MR Imaging of the Human Brain at 9.4 Tesla. *Proc. Intl. Soc. Mag. Reson. Med.* 18 (2010).

## ISMRM 2009 abstracts/presentations

1. Wiesner HM, Balla DZ, Pohmann R, Chen W, Ugurbil K, Uludag K.  $^{17}\text{O}$  T1/T2\* Tissue-Relaxation Rates with Anatomical Contrast in the Rat Brain at 16.4 T. *Proc. Intl. Soc. Mag. Reson. Med.* 18 (2010).
2. Zhu X-H, Zhang Y, Ugurbil K, Chen W. Direct and Noninvasive Measurement of Cerebral Metabolic Rate of ATP in Cat Brain and Its Physiological Implications. *Proc. Intl. Soc. Mag. Reson. Med.* 18 (2010).
3. McCommis KS, He X, Abendschein DR, Gupte PM, Gropler RJ, Zheng J. New Methods for the Quantification of Myocardial Oxygen Consumption with  $^{17}\text{O}$  MRI. *Proc. Intl. Soc. Mag. Reson. Med.* 18 (2010).
4. Atkinson IC, Thulborn KR. Non-Invasive, Whole-Brain CMRO<sub>2</sub> Mapping of the Human Brain. *Proc. Intl. Soc. Mag. Reson. Med.* 18 (2010).

## Reviews

1. Gordji-Nejad A, Mollenhoff K, Oros-Peusquens AM, Pillai DR, Shah NJ Characterizing cerebral oxygen metabolism employing oxygen-17 MRI/MRS at high fields, *Magn Reson Mater Phy* 2014; 27:81–93
2. Zhu XH, Zhang N, Zhang Y, Zhang X, Ugurbil K, Chen W. In vivo  $^{17}\text{O}$  NMR approaches for brain study at high field. *NMR Biomed.* Apr 2005;18(2):83-103.
3. Mateescu GD. Functional oxygen-17 magnetic resonance imaging and localized spectroscopy. *Adv Exp Med Biol.* 2003;510:213-8.

## Methods

1. Yuchi Liu, Yifan Zhang, Chunying Wu, Junqing Zhu, Charlie Wang, Nicholas Tomko, Mikhail D. Linetsky, Robert G. Salomon, Ciro Ramos-Estebanez, Yanming Wang and Xin Yu; High-Resolution Dynamic Oxygen-17 MR Imaging of Mouse Brain With Golden-Ratio-based Radial Sampling and k-Space-Weighted Image Reconstruction, *Magn. Reson. Med.*; Volume 79, Issue 1 January, 2018, Pages 256–263.
2. Sebastian C. Niesporek, Reiner Umathum, Jonathan M. Lommen, Nicolas G.R. Behl, Daniel Paech, Peter Bachert, Mark E. Ladd and Armin M. Nagel; Reproducibility of CMRO<sub>2</sub> determination using dynamic  $^{17}\text{O}$  MRI; *Magn Reson Med.* 2017 Oct 13. doi:10.1002/mrm.26952
3. Kurzhunov D, Borowiak R, Reisert M, Krafft AJ, Özen AC, Bock M. 3D CMRO<sub>2</sub> mapping in human brain with direct  $^{17}\text{O}$  MRI: comparison of conventional and proton-constrained reconstructions. *Neuroimage* 2017;155:612–624.
4. Kohsuke Kudo, Taisuke Harada, Hiroyuki Kameda, Ikuko Uwano, Fumio Yamashita, Satomi Higuchi, Kunihiro Yoshioka, Makoto Sasaki; Indirect MRI of  $^{17}\text{O}$ -labeled water using steady-state sequences: Signal simulation and preclinical experiment; *J. Magn. Reson. Imaging* 2017
5. Dmitry Kurzhunov, Robert Borowiak, Helge Hass, Philipp Wagner, Axel Joachim Krafft, Jens Timmer, Michael Bock Quantification of Oxygen Metabolic Rates in Human Brain With Dynamic  $^{17}\text{O}$  MRI: Profile Likelihood Analysis; *Magn Reson Med* 2016 Nov 1.
6. Lou S, Lepak VC, Eberly Le, Roth B, Cui W, Zhu XH, Öz G, Dubinsky JM.; Oxygen consumption deficit in Huntington disease mouse brain under metabolic stress.; *Hum Mol Genet.* 2016 Jul 1;25(13):2813-2826
7. Suzuki K, Igarashi H, Huber VJ, Kitaura H, Kwee IL, Nakada T.; Ligand-Based Molecular MRI: O-17 JJVCPE Amyloid Imaging in Transgenic Mice, *J Neurolmaging Epub* 23 FEB 2014
8. Zhu XH, Zhang Y, Wiesner HN, Ugurbil K, Chen W.; In Vivo Measurement of CBF Using  $^{17}\text{O}$  NMR Signal of Metabolically Produced H<sub>2</sub> $^{17}\text{O}$  as a Perfusion Tracer.; *Magn Res Medicine* 70:309–314 (2013)
9. Lu M, Zhang Y, Ugurbil K, Chen W, Zhu XH, In Vitro and In Vivo Studies of  $^{17}\text{O}$  NMR Sensitivity at 9.4 and 16.4 T.; *Magnetic Resonance in Medicine* 69:1523–1527 (2013)
10. Zhu XH, Chen JM, Tu TW, Chen W, Song SK Simultaneous and noninvasive imaging of cerebral oxygen metabolic rate, blood flow and oxygen extraction fraction in stroke mice, *NeuroImage* 64:437-447 (2013)
11. Hoffmann SH, Begovatz P, Nagel AM, et al.; A measurement setup for direct ( $^{17}\text{O}$ ) MRI at 7 T. *Magn Reson Med.* 2011;66(4):1109-15.
12. Hyder F.; Dynamic Brain Imaging Multi-Modal Methods and In Vivo Applications. 2009

13. Zhu XH, Du F, Zhang N, Zhang Y, Lei H, Zhang X, Qiao H, Ugurbil K, Chen W. Advanced In Vivo Heteronuclear MRS Approaches for Studying Brain Bioenergetics Driven by Mitochondria. *Methods Mol Biol.* 2009;489:317-57.
14. Mellon EA, Beesam RS, Kasam M, Baumgardner JE, Borthakur A, Witschey WR Jr, Reddy R. Single shot T1rho magnetic resonance imaging of metabolically generated water in vivo. *Adv Exp Med Biol.* 2009;645:279-86.
15. de Graaf RA, Brown PB, Rothman DL, Behar KL. Natural abundance  $^{17}\text{O}$  NMR spectroscopy of rat brain in vivo. *J Magn Reson.* 2008;193(1):63-7.
16. Thelwall PE. Detection of  $^{17}\text{O}$ -tagged phosphate by  $(31)\text{P}$  MRS: a method with potential for in vivo studies of phosphorus metabolism. *Magn Reson Med.* 2007;57(6):1168-72.
17. Zhu XH, Zhang Y, Zhang N, Ugurbil K, Chen W. Noninvasive and three-dimensional imaging of  $\text{CMRO}_2$  in rats at 9.4 T: reproducibility test and normothermia/hypothermia comparison study. *J Cereb Blood Flow Metab.* 2007; 27: 1225 – 1234.
18. Tailor DR, Baumgardner JE, Regatte RR, Leigh JS, Reddy R.; Proton MRI of metabolically produced  $\text{H}_2^{17}\text{O}$  using an efficient  $^{17}\text{O}_2$  delivery system. *Neuroimage.* 2004;22(2):611-618.
19. Sood R. Off-resonance binomial preparatory pulse technique for high sensitivity MRI of  $\text{H}_2\text{O}$ - $^{17}\text{O}$ . *Magn Reson Imaging.* 2004;22(2):181-195.
20. Fiat D, Hankiewicz J, Liu S, Trbovic S, Brint S.  $^{17}\text{O}$  magnetic resonance imaging of the human brain. *Neurol Res.* 2004;26(8):803-808.
21. Zhang X, Zhu XH, Tian R, Zhang Y, Merkle H, Chen W. Measurement of arterial input function of  $^{17}\text{O}$  water tracer in rat carotid artery by using a region-defined (REDE) implanted vascular RF coil. *MAGMA.* 2003;16 (2):77-85.
22. Zhu XH, Merkle H, Kwag JH, Ugurbil K, Chen W.  $^{17}\text{O}$  relaxation time and NMR sensitivity of cerebral water and their field dependence. *Magn Reson Med.* 2001;45(4):543-9.
23. Charagundla SR, Duvvuri U, Noyszewski EA, et al.  $^{17}\text{O}$ -decoupled  $(1)\text{H}$  spectroscopy and imaging with a surface coil: STEAM decoupling. *J Magn Reson.* 2000;143(1):39-44.
24. Reddy R, Stolpen AH, Charagundla SR, Insko EK, Leigh JS.  $^{17}\text{O}$ -decoupled  $^1\text{H}$  detection using a double-tuned coil. *Magn Reson Imaging.* 1996;14(9):1073-1078.
25. Reddy R, Stolpen AH, Leigh JS. Detection of  $^{17}\text{O}$  by proton T1 rho dispersion imaging. *J Magn Reson B.* 1995;108(3):276-279
26. Lasker SE. Functional MR imaging of a metabolite of  $^{17}\text{O}_2$ . *Artif Cells Blood Substit Immobil Biotechnol.* 1994;22(4):1055-68.
27. Ronen I, Navon G. A new method for proton detection of  $\text{H}_2^{17}\text{O}$  with potential applications for functional MRI. *Magn Reson Med.* 1994;32(6):789-793.
28. Kwong KK, Xiong J, Kuan WP, Cheng HM. Measurement of water movement in the rabbit eye in vivo using  $\text{H}_2^{17}\text{O}$ . *Magn Reson Med.* 1991;22(2):443-50.
29. Hopkins AL, Haacke EM, Barr RG, Tkach J. Oxygen-17 contrast agents. Fast imaging techniques. *Invest Radiol.* 1988;23 Suppl 1:S240-242.
30. Hopkins AL, Barr RG. Oxygen-17 compounds as potential NMR T2 contrast agents: enrichment effects of  $\text{H}_2^{17}\text{O}$  on protein solutions and living tissues. *Magn Reson Med.* 1987;4(4):399-403.
31. Yeung HN, Lent AH. Proton transverse relaxation rate of  $^{17}\text{O}$ -enriched water. *Magn Reson Med.* 1987;5(1):87

## Brain

1. Yuchi Liu, Yifan Zhang, Chunying Wu, Junqing Zhu, Charlie Wang, Nicholas Tomko, Mikhail D. Linetsky, Robert G. Salomon, Ciro Ramos-Estebanez, Yanming Wang and Xin Yu; High-Resolution Dynamic Oxygen-17 MR Imaging of Mouse Brain With Golden-Ratio-Based Radial Sampling and k-Space-Weighted Image Reconstruction; *Magnetic Resonance in Medicine* 79:256–263 (2018)
2. Marie-Aline Neveu, Nicolas Joudiou, Géraldine De Preter, Jean-Paul Dehoux, Bénédicte F. Jordan and Bernard Gallez;  $^{17}\text{O}$  MRS assesses the effect of mild hypothermia on oxygen consumption rate in tumors; *NMR in Biomedicine, Vol. 30, Issue 8, Aug. 2017*
3. Kohsuke Kudo, Taisuke Harada, Hiroyuki Kameda, Ikuko Uwano, Fumio Yamashita, Satomi Higuchi, Kunihiro Yoshioka, Makoto Sasaki; Indirect Proton MR Imaging and Kinetic Analysis of  $^{17}\text{O}$ -Labeled Water Tracer in the Brain; *Magn Reson Med Sci* 2017; doi:10.2463/mrms.mp.2017-0094

4. Xiao-Hong Zhu, Wei Chen ; In vivo  $^{17}\text{O}$  MRS imaging – Quantitative assessment of regional oxygen consumption and perfusion rates in living brain; *Analytical Biochemistry* Vol. 529, 15 July 2017, Pages 171-178.
5. Hannes M. Wiesner, Dávid Z. Balla, G. Shajan, Klaus Scheffler, Kâmil Uğurbil, Wei Chen, Kâmil Uludağ and Rolf;  $^{17}\text{O}$  relaxation times in the rat brain at 16.4 tesla; *Magnetic Resonance in Medicine* Vol. 75, 5, 1886–1893, May 2016
6. DeLaPaz R, Gupte P.; Potential Application of  $^{17}\text{O}$  MRI to Human Ischemic Stroke. *Adv Exp Med Biol.* 2011;701:22
7. Mellon EA, Beesam RS, Elliott MA, Reddy R.; Mapping of cerebral oxidative metabolism with MRI. *Proc Natl Acad Sci U S A.* 2010;107(26):11787-92
8. Atkinson IC, Sonstegaard R, Pliskin NH, Thulborn KR. Vital signs and cognitive function are not affected by  $^{23}\text{Na}$  and  $^{17}\text{O}$  magnetic resonance imaging of the human brain at 9.4 T. *J Magn Reson Imaging.* 2010;32(1):82-7.
9. Atkinson IC, Thulborn KR. Feasibility of mapping the tissue mass corrected bioscale of cerebral metabolic rate of oxygen consumption using  $^{17}\text{O}$ -oxygen and  $^{23}\text{Na}$ -sodium MR imaging. *Neuroimage.* 2010;51(2):723-33.
10. Zhu X-H, Zhang N, Zhang Y, Ugurbil K, Chen W. New insights into central roles of cerebral oxygen metabolism in the resting and stimulus-evoked brain. *J Cereb Blood Flow Metab.* 2009;29(1):10–8.
11. Mellon EA, Beesam RS, Baumgardner, Borthakur A, Witschey WR, Reddy R. Estimation of the regional cerebral metabolic rate of oxygen consumption with proton detected  $^{17}\text{O}$  MRI during precision  $^{17}\text{O}_2$  inhalation in swine. *J Neurosci Methods.* 2009;179(1):29-39.
12. Mellon EA, Beesam RS, Baumgardner JE, Borthakur A, Witschey WR, Reddy R. Estimation of the regional cerebral metabolic rate of oxygen consumption with MRI during the first 60 seconds of  $^{17}\text{O}_2$  inhalation in swine. *Proc. Intl. Soc. Mag. Reson. Med.* 16 (2008).
13. Zhu XH, Zhang Y, Zhang N, Ugurbil K, Chen W., Noninvasive and three-dimensional imaging of CMRO<sub>2</sub> in rats at 9.4 T: reproducibility test and normothermia/hypothermia comparison study. *J. Cereb Blood Flow Metab.* 2007;27(6):1225-34
14. Tailor DR, Roy A, Regatte RR, et al. Indirect  $^{17}\text{O}$ -magnetic resonance imaging of cerebral blood flow in the rat. *Magn Reson Med.* 2003;49(3):479-487.
15. DeLaPaz RL, Gupte P, Connolly S, Wu E, Brown T. Oxygen-17 Uptake in Mouse Cerebral Ischemia. *Proc. Intl. Soc. Mag. Reson. Med.* 11 (2003).
16. de Crespigny AJ, D'Arceuil HE, Engelhorn T, Moseley ME. MRI of focal cerebral ischemia using  $^{17}\text{O}$ -labeled water. *Magn Reson Med.* 2000;43(6):876-883.
17. Ronen I, Merkle H, Ugurbil K, Navon G. Imaging of  $\text{H}_2^{17}\text{O}$  distribution in the brain of a live rat by using proton-detected  $^{17}\text{O}$  MRI. *Proc Natl Acad Sci U S A.* 1998; 95 (22):12934-12939.
18. Arai T, Nakao S, Morikawa S, et al. Measurement of local cerebral blood flow by magnetic resonance imaging: in vivo autoradiographic strategy using  $^{17}\text{O}$ -labeled water. *Brain Res Bull.* 1998;45(5):451-456.
19. Pekar J, Sinnwell T, Ligeti L, Chesnick AS, Frank JA, McLaughlin AC. Simultaneous measurement of cerebral oxygen consumption and blood flow using  $^{17}\text{O}$  and  $^{19}\text{F}$  magnetic resonance imaging. *J Cereb Blood Flow Metab.* 1995;15(2):312-320.
20. Fiat D, Dolinsek J, Hankiewicz J, Dujovny M, Ausman J. Determination of regional cerebral oxygen consumption in the human:  $^{17}\text{O}$  natural abundance cerebral magnetic resonance imaging and spectroscopy in a whole body system. *Neurol Res.* 1993;15(4):237-48.
21. Fiat D, Kang S. Determination of the rate of cerebral oxygen consumption and regional cerebral blood flow by non-invasive  $^{17}\text{O}$  in vivo NMR spectroscopy and magnetic resonance imaging. Part 2. Determination of CMRO<sub>2</sub> for the rat by  $^{17}\text{O}$  NMR, and CMRO<sub>2</sub>, rCBF and the partition coefficient for the cat by  $^{17}\text{O}$  MRI. *Neurol Res.* 1993;15(1):7-22
22. Fiat D, Ligeti L, Lyon RC, et al. In vivo  $^{17}\text{O}$  NMR study of rat brain during  $^{17}\text{O}_2$  inhalation. *Magn Reson Med.* 1992;24(2):370-374.
23. Kwong KK, Hopkins AL, Belliveau JW, et al. Proton NMR imaging of cerebral blood flow using  $\text{H}_2^{17}\text{O}$ . *Magn Reson Med.* 1991;22(1):154-158.
24. Hopkins AL, Lust WD, Haacke EM, Wielopolski P, Barr RG, Bratton CB. The stability of proton T2 effects of oxygen-17 water in experimental cerebral ischemia. *Magn Reson Med.* 1991;22(1):167-174.

25. Pekar J, Ligeti L, Ruttner Z, Lyon RC, Sinnwell TM, van Gelderen P, Fiat D, Moonen CT, McLaughlin AC. In vivo measurement of cerebral oxygen consumption and blood flow using  $^{17}\text{O}$  magnetic resonance imaging. *Magn Reson Med*. 1991;21(2):313-9.
26. Arai T, Mori K, Nakao S, Watanabe K, Kito K, Aoki M, Mori H, Morikawa S, Inubushi T. In vivo Oxygen-17 nuclear magnetic resonance for the estimation of cerebral blood flow and oxygen consumption. *Biochem Biophys Res Commun*. 1991;179(2):954-61.
27. Arai T, Nakao S, Mori K, et al. Cerebral oxygen utilization analyzed by the use of Oxygen-17 and its nuclear magnetic resonance. *Biochem Biophys Res Commun*. 1990;169(1):153-158.
28. Hopkins AL, Haacke EM, Tkach J, Barr RG, Bratton CB. Improved sensitivity of proton MR to Oxygen-17 as a contrast agent using fast imaging: detection in brain. *Magn Reson Med*. 1988;7(2):222-229.

### Miscellaneous

1. Samuel A. Einstein, Bradley P. Weegman, Jennifer P. Kitzmann, Klearchos K. Papas, Michael Garwood; Noninvasive assessment of tissue-engineered graft viability by oxygen-17 magnetic resonance spectroscopy; *Biotechnology and Bioengineering*, Vol 114, Issue 5, May 2017, 1118-1121.
2. Borowiak R, Groebner J, Haas M, Hennig J, Bock M, Direct cerebral and cardiac  $^{17}\text{O}$ -MRI at 3 Tesla: initial results at natural abundance, *Magn Reson Mater Phy* 2014; 27:95–99
3. Lu M, Atthe B, Mateescu G, Flaska CA, Yua X, Assessing mitochondrial respiration in isolated hearts using  $^{17}\text{O}$  MRS NMR *Biomed* 2012; 25(6): 883–889
4. McCommis KS, He X, Abendschein DR, Gupte PM, Gropler RJ, Zheng J. Cardiac  $^{17}\text{O}$  MRI: Toward Direct Quantification of Myocardial Oxygen Consumption. *Magn Reson Med*. 2010;63(6):1442-7.
5. Rogers WJ, Gupte PM, Piccione EA, Kramer CM, Vido DA, Reichek N. T2 Imaging Using O-17 for Detection of Viability in Myocardial Infarction. *Proc. Intl. Soc. Mag. Reson. Med*. 7 (1999).
6. Fung BM, McGaughy TW. Study of spin-lattice and spin-spin relaxation times of  $^1\text{H}$ ,  $^2\text{H}$ , and  $^{17}\text{O}$  in muscular water. *Biophys J*. 1979;28(2):293-303.
7. Civan MM, Shporer M. Pulsed nuclear magnetic resonance study of  $^{17}\text{O}$ ,  $^2\text{D}$ , and  $^1\text{H}$  of water in frog striated muscle. *Biophys J*. 1975;15(4):299-306.
8. Hoffmann SH, Radbruch A, Bock M, Semmler W, Nagel AM, Direct  $^{17}\text{O}$  MRI with partial volume correction: first experiences in a glioblastoma patient, *Magn Reson Mater Phy*; epub April 1, 2014
9. Narazaki M, Kanazawa Y, Koike S, Ando K, Ikehira H. Dynamical  $^{17}\text{O}$  imaging in tumor bearing mice at 7T. *Proc. Intl. Soc. Mag. Reson. Med*. 15 (2007).
10. Tailor DR, Poptani H, Glickson JD, Leigh JS, Reddy R. High-resolution assessment of blood flow in murine RIF-1 tumors by monitoring uptake of  $\text{H}_2^{17}\text{O}$  with proton T(1rho)-weighted imaging. *Magn Reson Med*. 2003;49 (1):1-6.
11. Shporer M, Haas M, Civan MM. Pulsed nuclear magnetic resonance study of  $^{17}\text{O}$  from  $\text{H}_2^{17}\text{O}$  in rat lymphocytes. *Biophys J*. 1976;16(6):601-11.

# Our cooperation partner

## Polarean Imaging plc.

Located in the Research Triangle Park area of North Carolina, Polarean Imaging plc. designs and manufactures equipment for production of hyperpolarized Xenon or Helium gas.

Polarean Imaging plc (AIM: POLX), the medical-imaging technology company, with a proprietary drug-device combination product for the magnetic resonance imaging (MRI) market, notes the publication of a study using Polarean's hyperpolarised gas MRI technology in a study of patients with severe asthma in the April edition of the American Journal of Respiratory and Critical Care Medicine (AJRCCM).

**The 9820  $^{129}\text{Xe}$  hyperpolarizer** provides a routine supply of high-purity, hyperpolarized  $^{129}\text{Xe}$  for gas phase magnetic resonance studies. The polarizer is typically installed near the MRI/NMR suite and processes a custom mixture of  $^{129}\text{Xe}$ ,  $\text{N}_2$ , and  $^4\text{He}$ , into one or more doses of pure hyperpolarized  $^{129}\text{Xe}$  that is available for magnetic resonance studies. There is no chemical change associated with hyperpolarization – only nuclear spin alignment and cryogenic extraction of pure xenon. The hyperpolarized  $^{129}\text{Xe}$  is then thawed and dispensed into a container or bag. Once dispensed into an appropriate container, and maintained within a modest holding magnetic field, the polarization relaxes with a  $T_1$  of 1–2 hr.

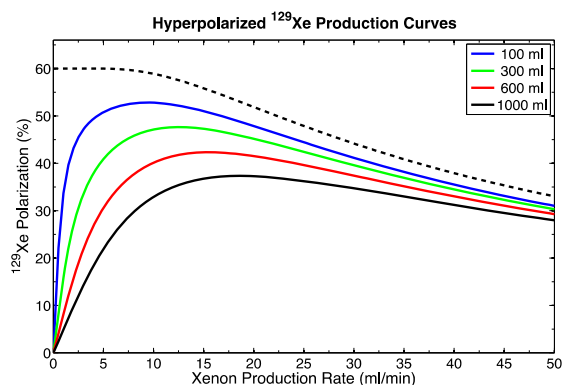


*The new generation 9820 xenon polarizer features a tunable 200W water-cooled narrowed linewidth laser, an expanded oven to accommodate substantially larger volume cells, and a 4-coil electromagnetic field configuration to provide uniform coverage over the oven and polarized gas plumbing.*

### System Overview and Specifications

The 9820 Xenon Hyperpolarization system can be operated on site by personnel who have undergone appropriate training. Polarization levels range over 35–45% depending on the volume and throughput of produced xenon, typically at 1–3 L/h. The system operates as a Class 1 laser, and thus requires no laser protective eyewear during normal operation.

**Note:** The 9820 Xenon Hyperpolarization system is designed for research use. If the system is used to produce hyperpolarized  $^{129}\text{Xe}$  for human inhalation, all applicable institutional and federal approvals must be obtained.



The 9820 xenon polarizer is capable of delivering  $^{129}\text{Xe}$  polarization levels in the range of 35–45% as a function of production rate (1–3 L/h) when operating at the peak laser power. The dashed line shows the typical  $^{129}\text{Xe}$  polarization leaving a 1.5-L cell whereas the color-coded lines depict the collected xenon volume using an effective solid-state xenon relaxation time of one hour.



The standard 9820 xenon polarizer configuration comes with a 1.5-L optical pumping cell, a triple-zone temperature control system, custom optics to deliver a highly uniform laser beam across the entire cell length, and a high efficiency cryogenic xenon collection system. The 9820 platform is designed with several expansion options to enhance performance and throughput as new components become available. In the picture above, oven and laser covers are removed to show the details.

### System Components

- Custom hyperpolarized  $^{129}\text{Xe}$  compatible valves and tubing
- Hyperpolarized  $^{129}\text{Xe}$  collection plumbing within the electromagnetic field
- Narrowed linewidth tunable 200W 795-nm optical pumping laser in Class 1 housing

- Circular polarizing and beam collimating optics
- Mass flow and pressure transducers
- Closed circuit water chiller for robust temperature control
- High-field high-capacity cryogenic accumulation area
- Vacuum pump and purge function to prepare delivery containers
- Shielded oven with dual-action active heating/cooling temperature control
- Flow-through optical cell installed in series with rubidium pre-saturator each with its own dedicated temperature control
- Laser transmission and spectral monitoring
- Safety interlocks
- Central power distribution

### Safety Features

- Filtered power distribution
- Air flow switch
- Interlocked protective laser housing for Class 1 operation
- CE Mark, UL and CSA approvals
- DOT approved shipping of replacement optical cells.

### Optional Equipment and Services

- Polarization measurement station with absolute calibration for  $^3\text{He}$  and  $^{129}\text{Xe}$
- Dual source  $^{129}\text{Xe}$  cylinder manifold for real-time switching between natural abundance and enriched xenon mixes. This minimizes the risk of system contamination and downtime during frequent xenon cylinder changes.
- Heavy duty external purifier module with bypass function installed between the external gas manifold and the polarizer in order to further purify the gas mixes, protect the system against potential contamination and prolong the life of optical cells at their peak performance.
- Dose mixing syringes

### Laboratory Space Requirements

- Controlled access space capable of temporary Class 4 laser operations
- Minimum room dimensions:
  - width 120" (3m)
  - depth 84" (2m)
  - height 84" (2m)
- Ferrous materials to be at least 3' (1m) away from the polarizer.
- Local ambient magnetic field preferably less than 1 Gauss

### Polarizer Dimensions

- 170cm L x 60cm W x 160cm H
- (65" L x 24" W x 60" H)

### Electrical Requirements

- 3 phase 208 V, 47-63 Hz, 20 A per phase
- Power outlet: US NEMA L21-30R
- Lockable isolate box

### Compressed Air

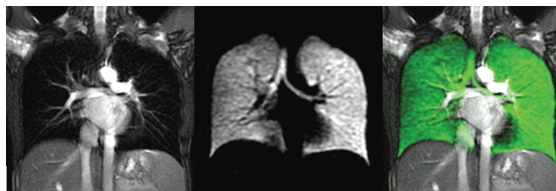
- 20 psig (1.5 bar) minimum pressure
- 4 standard cubic feet per minute (110 L/min) minimal flow
- 0.01% water maximal content

### Environmental Requirements

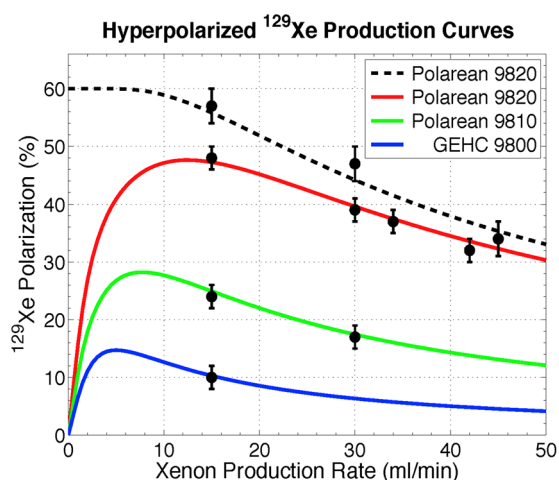
- 5 kW/h maximal heat load (17,000 BTUH = 1.5 Ton)
- Room temperature between 68-75 °F (20-24 °C)
- Dedicated temperature control

### Supplies and Consumables

- External  $^{129}\text{Xe}$ - $^4\text{He}$ - $\text{N}_2$  tank
- External UHP  $\text{N}_2$  tank
- External commercial  $\text{N}_2$  tank
- Liquid nitrogen
- Dose delivery bags



A pioneer in hyperpolarized gas systems, Polarean, Inc. is opening new avenues for functional and physiological imaging with its hyperpolarized gas MRI technology. High-resolution, 3D images of inhaled noble gases using conventional MRI scanners illuminate tissue characteristics and organ function currently inaccessible by existing methods. Hyperpolarized gases provide a promising research platform to extend MRI capabilities.



*Predicted  $^{129}\text{Xe}$  polarization level for a 300-ml batch after freeze-thaw as a function of flow for different polarizer generations. Dashed line shows xenon polarization leaving the optical cell in 9820 polarizer using a 200W laser. Data points show experimental values.*

**POLAREAN**

PO Box 14805  
Research Triangle Park, NC 27709-4805  
United States

Phone: +1-(919)-206-7900

Fax: +1-(919)-206-7901

[info@polarean.com](mailto:info@polarean.com)

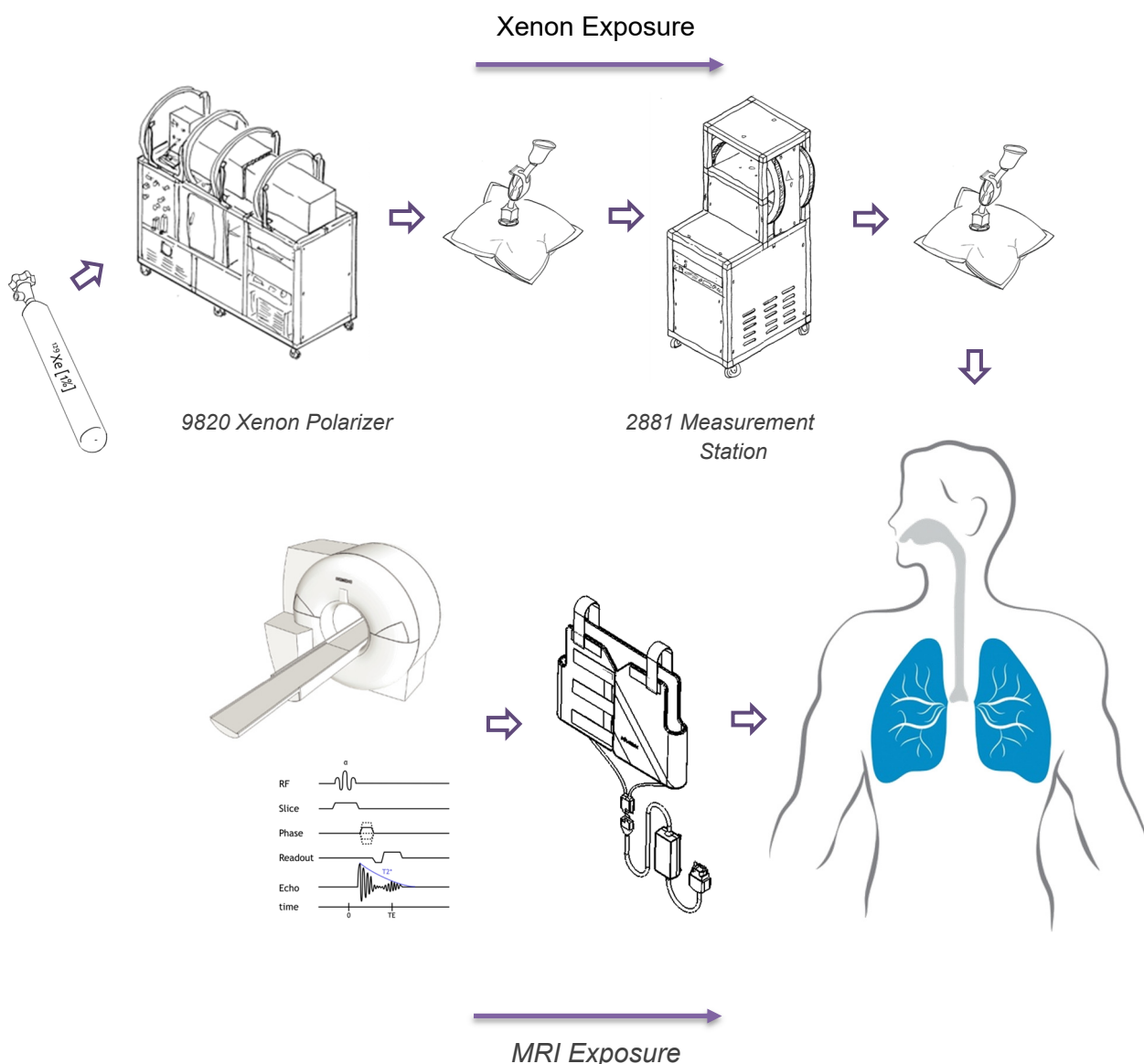
## How does imaging with hyperpolarized Xe-129 work?

Hyperpolarized Xenon-129 magnetic resonance (MR) is a powerful “tool” to study pulmonary function and lung structure in ways, that are not possible with other research modalities.

Hyperpolarization of  $^{129}\text{Xe}$  is accomplished by placing a non-radioactive isotope of the Xenon source gas into a beam of polarized laser light in the presence of very small amounts of an alkali metal. The result is Xenon whose nuclear magnetic spin is highly aligned, but not chemically or biologically different than un-polarized Xenon, a harmless inert gas.

Once the Xenon-129 is hyperpolarized, it can be dispensed in a plastic bag, the amount of polarized gas is verified and then it is administered to the subject already lying down inside the MRI scanner. The patient inhales a small quantity (a few hundred ml) of the gas and undergoes a MRI scan. The MRI scan is typically completed within a 10-20 second breath hold.

Compared to air that is typically within the lung, the hyperpolarized Xenon enhances the MRI signal by a factor of 100,000 making lung structure and regional ventilation exquisitely visible.



For further detailed information, please visit:

<http://www.polarean.com>

# Our ISMRM rubber duck family

Due to the great interest in our rubber ducks, we are pleased to introduce our ducks from the previous ISMRM conferences.

The ducks are not for sale and only available at our booth (#811).

*Come and visit us to pick up your 2019<sup>th</sup> duck.*



**Dr. Jacques**

Montreal 2019 – 27<sup>th</sup> ISMRM

## Our ISMRM rubber duck family



**Dr. Amy**

Paris 2018



**Nurse Xenia**

Hawaii 2017



**Nurse Gudrun**

Singapore 2016



**Dr. Willy**

Toronto 2015



**Nurse Alberta**

Salt Lake City 2013



**Nurse Roberta**

Melbourne 2012



**Dr. Bob (Robert)**

Montreal 2011



**NUKEM Isotopes Imaging GmbH**

Rodenbacher Str. 47

63755 Alzenau, Germany

E: [info@nukemisotopes.de](mailto:info@nukemisotopes.de)

[www.nukemisotopes.de](http://www.nukemisotopes.de)